



AFRL-OSR-VA-TR-2015-0097

---

## HIGHER-ORDER MOTION INPUTS FOR VISUAL FIGURE TRACKING

Patrick Shoemaker  
TANNER RESEARCH, INC

---

04/03/2015  
Final Report

DISTRIBUTION A: Distribution approved for public release.

Air Force Research Laboratory  
AF Office Of Scientific Research (AFOSR)/ RSL  
Arlington, Virginia 22203  
Air Force Materiel Command

<b>REPORT DOCUMENTATION PAGE</b>					Form Approved OMB No. 0704-0188	
<p>The public reporting burden for this collection of information is estimated to average 1 hour per response, including the time for reviewing instructions, searching existing data sources, gathering and maintaining the data needed, and completing and reviewing the collection of information. Send comments regarding this burden estimate or any other aspect of this collection of information, including suggestions for reducing the burden, to Department of Defense, Executive Services, Directorate (0704-0188). Respondents should be aware that notwithstanding any other provision of law, no person shall be subject to any penalty for failing to comply with a collection of information if it does not display a currently valid OMB control number.</p> <p>PLEASE DO NOT RETURN YOUR FORM TO THE ABOVE ORGANIZATION.</p>						
<b>1. REPORT DATE (DD-MM-YYYY)</b> 04-05-2015		<b>2. REPORT TYPE</b> Final Performance		<b>3. DATES COVERED (From - To)</b> 01-12-2011 to 31-05-2015		
<b>4. TITLE AND SUBTITLE</b> HIGHER-ORDER MOTION INPUTS FOR VISUAL FIGURE TRACKING: CONTROL ALGORITHMS AND NEURAL CIRCUITS				<b>5a. CONTRACT NUMBER</b>		
				<b>5b. GRANT NUMBER</b> FA9550-12-1-0034		
				<b>5c. PROGRAM ELEMENT NUMBER</b>		
<b>6. AUTHOR(S)</b> Patrick Shoemaker				<b>5d. PROJECT NUMBER</b>		
				<b>5e. TASK NUMBER</b>		
				<b>5f. WORK UNIT NUMBER</b>		
<b>7. PERFORMING ORGANIZATION NAME(S) AND ADDRESS(ES)</b> TANNER RESEARCH, INC 825 S MYRTLE AVE MONROVIA, CA 91016 - 3424 US				<b>8. PERFORMING ORGANIZATION REPORT NUMBER</b>		
<b>9. SPONSORING/MONITORING AGENCY NAME(S) AND ADDRESS(ES)</b> AF Office of Scientific Research 875 N. Randolph St. Room 3112 Arlington, VA 22203				<b>10. SPONSOR/MONITOR'S ACRONYM(S)</b> AFOSR		
				<b>11. SPONSOR/MONITOR'S REPORT NUMBER(S)</b>		
<b>12. DISTRIBUTION/AVAILABILITY STATEMENT</b> A DISTRIBUTION UNLIMITED: PB Public Release						
<b>13. SUPPLEMENTARY NOTES</b>						
<b>14. ABSTRACT</b> <p>Visual figures are detectable based on a range of spatiotemporal characteristics that differ from surrounding background. A figure that corresponds to an ordinary moving object generates coherent two-point space-time correlations related to the first moment of the luminance distribution. Such signals are readily detectable by the standard implementation of the Hassenstein-Reichardt elementary motion detector (EMD), and as such are referred to here as EM. By contrast, figures defined by the second or higher-order moments, the envelope, or</p>						
<b>15. SUBJECT TERMS</b> <p>visual figure tracking</p>						
<b>16. SECURITY CLASSIFICATION OF:</b>			<b>17. LIMITATION OF ABSTRACT</b>	<b>18. NUMBER OF PAGES</b>	<b>19a. NAME OF RESPONSIBLE PERSON</b> Patrick Shoemaker	
<b>a. REPORT</b>	<b>b. ABSTRACT</b>	<b>c. THIS PAGE</b>			<b>19b. TELEPHONE NUMBER (Include area code)</b> 626-471-9786	
U	U	U	UU			

**FA9550-12-1-0034**

---

## **Higher-Order Inputs for Visual Figure Tracking: Control Algorithms and Neural Circuits**

**Final Report**  
**May 30, 2015**

**Patrick Shoemaker**

Tanner Research, Inc.  
825 South Myrtle Ave.  
Monrovia CA 91016  
USA  
(626) 471-9786

**Karin Nordström**

Department of Neuroscience  
Uppsala University  
Husargatan 3  
751 24 Uppsala  
Sweden  
+46 18 471 4171

**Mark Frye**

Howard Hughes Medical Institute  
Department of Integrative Biology and Physiology  
University of California, Los Angeles  
610 Charles Young Dr. East  
Los Angeles CA 90095  
USA  
(310) 825-5360

**Approved for public release; distribution is unlimited**

## Contents

1	Abstract .....	3
2	Objectives .....	3
3	Accomplishments / New Findings .....	3
3.1	Introduction and Background .....	3
3.2	Experimental and Analytical Techniques .....	4
3.3	Behavior .....	5
3.3.1	The STAF as a characterization of behavioral responses to figures .....	6
3.3.2	Filters for visual figure-ground discrimination .....	9
3.3.1	A figure edge is coded by the higher-order FM pathway .....	11
3.3.2	Figure tracking and threat avoidance by the FM system .....	12
3.3.3	STAFs in the frequency domain and figure tracking microsaccades .....	14
3.4	Electrophysiology .....	17
3.4.1	Sensitivity to higher-order motion in the LPTCs .....	17
3.4.2	Figure-ground discrimination in hoverfly LPTCs .....	20
3.4.3	Centrifugal stationary inhibited flicker excited (cSIFE) Neuron .....	24
3.5	In-Vivo Imaging .....	28
3.6	Mechanisms and Models .....	31
3.6.1	Context established by initial work .....	31
3.6.2	Modeling of cSIFE .....	32
3.6.3	Modeling of biophysically-plausible ‘delay’ and ‘correlate’ mechanisms .....	33
3.6.4	Fundamental computations underlying figure detection .....	37
3.6.5	Winner-takes-all neural circuit with NMDA receptors .....	43
4	Personnel Supported .....	49
5	Publications .....	49
5.1	Peer-Reviewed Publications Fully or Partially Supported by this Grant: .....	49
	Papers Submitted or in Production, Fully or Partially Supported by this Grant: .....	50
5.2	Papers by the Principals in Related Areas: .....	50
6	Interactions / Transitions .....	51
6.1	Participation/presentation at meetings, conferences, and seminars .....	51
6.1.1	Service on Organizing Committees for Meetings: .....	51
6.1.2	Conference Presentations / Posters: .....	51
6.2	Consultative and advisory functions .....	52
6.3	Transitions .....	53
7	New Discoveries, Inventions, or Patent Disclosures .....	53
8	Honors / Awards .....	53
	References .....	53



## 1 Abstract

Visual figures are detectable based on a range of spatiotemporal characteristics that differ from surrounding background. A figure that corresponds to an ordinary moving object generates coherent two-point space-time correlations related to the first moment of the luminance distribution. Such signals are readily detectable by the standard implementation of the Hassenstein-Reichardt elementary motion detector (EMD), and as such are referred to here as EM. By contrast, figures defined by the second or higher-order moments, the envelope, or variance of the luminance distribution evade detection by an EMD, yet are readily perceptible to humans and non-human primates, and are thought to be processed through distinct cortical streams. The project participants have demonstrated that flies process higher-order signals for feature detection, and now others in the field are beginning to ‘see the light’ as it were, demonstrating perceptual capabilities in flies that rival any revealed in the human psychophysics literature. It would appear that even the most complex visual motion signals, including those that defeat the standard implementation of the EMD, are encoded and perceived by flies without the computational overhead (or experimental intractability) of cortical processing. Under support of this grant, our group has shed light on the computational input-output filters and underlying neural foci of higher-order motion vision in flies, and begun to propose mechanisms and models that extend current understanding of the associated visual processing. These findings we expect to be broadly applicable to all high-performance vision systems, both biological and engineered. In the process, seventeen manuscripts have been published, are under review, or in production for the peer-reviewed literature, as a result of the grant.

## 2 Objectives

The central objective of the project is an understanding of the quantitative systems algorithms and underlying neural circuits that enable flies to robustly code and actively track complex visual figures against cluttered and dynamic visual backgrounds in flight. In pursuit of this objective, we aim to answer three broad questions:

1. What are the higher-order spatial and temporal statistical characteristics of visual features that drive active figure tracking?
2. What is the neural substrate for the detection of higher-order figures, and what are the computational algorithms?
3. What is the relationship between figure detection and other forms of visual motion processing, in particular wide-field motion processing and small target detection, and in what ways may they be distinguished?

There were no changes to these objectives or aims during the course of the project.

## 3 Accomplishments / New Findings

### 3.1 Introduction and Background

The detection of first order visual motion in biology is well studied, both behaviorally and physiologically. Even if motion could theoretically be computed in a variety of ways, to date essentially all animals investigated appear to detect local motion in fundamentally the same way (for a recent review, see [9]). In local elementary motion detectors (EMDs), luminance changes from two neighboring inputs are correlated after delaying the signal from one of the inputs. By

subtracting the output from a mirror symmetric subunit, direction-selective local motion sensitivity is generated. In the vertebrate visual cortex, and the fly lobula plate, neurons with large dendritic trees are believed to sample the input from many of such local EMDs, thereby generating wide-field direction-selectivity to the types of optic flow generated during egomotion.

The detection of first-order, or *Fourier*, motion thus relies on the presence of a coherent correlation of luminance across space and time, and forms the theoretical basis for the classic EMD model of Hassenstein and Reichardt [24]. However, general motion signals in nature do not always form clean space-time correlations, but may also be comprised of higher-order signals related to changes in contrast or texture, for example when viewing a distant, near-stationary scene through a gap in the foliage while moving past that gap, or viewing an object that moves in and out of shadows. The term *higher-order motion* refers to movement of visual objects in which internal first-order motion cues do not correspond with object motion. Such an object might have no net motion energy (i.e., without Fourier motion components [14]), or contain paradoxical motion cues. Stimuli of the first type are referred to as *drift-balanced*, and in our experiments comprise a moving object containing an internal pattern that varies from and replaces the background as the object moves, but which itself is non-moving. Drift-balanced stimuli do not contain cues that are encodable by standard EMDs (although some degree of sensitivity can be imparted by adding a front-end non-linearity to the EMD, such as a half-wave, or full-wave, rectifier, or a high-pass filter [14][61]).

Theta motion [62] is a second class of higher-order motion in which a moving object contains an internal pattern that moves coherently in the direction opposite to the object itself. In this case, an EMD would encode the motion of the internal pattern (elementary motion, *EM*) and not the motion of the object (figure motion, *FM*). Theobald et al. [55] showed that fruit flies track not only Fourier bars, as expected by a visual system depending on EMD-type input [10], but that they also track drift-balanced bars and theta bars, showing that cortical processing is not needed for higher-order motion sensitivity. The demonstrated sensitivity to higher-order motion [55][57] is highly counter-intuitive as such signals cannot be encoded by the standard EMD [14], and they would thus not be expected to be detectable at all by motion processing computations in the fly. The mere fact that such computations are made even by such a small brain highlights the importance of the underlying algorithms for high-performance vision. Our research aims to increase the understanding of the behavior and neural circuits associated with these algorithms.

Aptekar and Frye have published a critique of the current literature that demonstrates broad parallels in the computations being made in fly and human vision [1]. In particular, we highlighted motion stimuli that cannot be distinguished by the standard implementation of the elementary motion detector (EMD), including reverse-phi, plaids, and theta bars, all three of which have been first been demonstrated in humans, and now also in flies. It would appear that highly complex motion computations are conserved across species separated by hundreds of millions of years of evolution, implying that high performance motion vision computations are rapid, compact, and prevalent.

### 3.2 Experimental and Analytical Techniques

A major area of progress in this area has been in the application white noise or m-sequence techniques for system identification to whole animal behavior in response to the motion of various classes of visual figures. The Frye lab initiated the use of such white-noise techniques in behavioral studies of flies [13][56], and we first applied them to the problem of visual figure detection under a prior AFOSR grant (FA9550-09-1-0116) [55]. Under the current grant, we have significantly expanded this application to the domain of figure detection and its role in fly

optomotor responses [4][20][21], in the process introducing the space-time representations we call Spatio-Temporal Action Fields, or *STAFs*, which are named for their similarity to Spatio-Temporal Receptive Fields (STRFs) widely used in electrophysiology. STAFs characterize open-loop motor response of the fly to EM and FM components of figure motion; the STAF concept has now been extended to characterize both compound figure and background motion, and head movement during figure tracking as well.

During pursuit of this work we have developed numerical techniques to increase the accuracy of estimation of STAFs, adapted and refined experimental / analytical techniques for use with these novel aspects of optomotor figure responses, and (motivated in part by the review process on submitted manuscripts) advanced the general understanding of their proper application as well as limitations. Our perception is that this work has generated interest in other vision science laboratories – but in addition, a healthy skepticism about the overall approach. In response, we have undertaken an effort to rigorously document the technique and its theoretical underpinnings, relying for examples on its application our peer reviewed studies. As part of this work, a student in the Frye lab (P. Lu) performed experiments with flies in which optomotor responses were characterized for both control animals and flies with eyes painted over, as further illustration of the technique and the information it can provide. This methodology paper has been published (with associated Matlab software) in the journal *Frontiers in Neural Circuits* [2].

New genetic techniques available in *Drosophila* provide a powerful tool for targeting various classes of neurons for the expression of fluorescent proteins for imaging purposes, or of inhibitory ion channels for purposes of ‘knocking’ out cells by shunting of excitatory potentials. During the latter part of the grant, we have used two-photon excitation calcium imaging in conjunction with such genetic techniques to target and examine the responses of specific cell types *in vivo* to various types of figure and edge-related stimuli.

Despite the genetic tools available in *Drosophila*, larger flies are more amenable to intracellular electrophysiology, which allows the assessment of subtle, but important, inhibitory and excitatory signals. As such, many questions are still better addressed in the larger model organisms, and thus we have pursued electrophysiological study in the element of the grant addressed by the Nordström lab. This work has focused on recordings in the lobula plate to investigate the neural substrate underlying higher-order motion sensitivity, and the responses to figure-ground stimuli. Furthermore, we have searched for and identified novel, previously undescribed neurons in the fly lobula plate.

### 3.3 Behavior

In psychophysical studies through the decades, photoreceptor-sized displacements of a luminous edge have revealed elementary mechanisms of motion vision in insects and vertebrates. By contrast, our behavioral work has explored the extreme performance limits of motion vision in flies. Using various ‘virtual reality’ simulators, the Frye lab discovered that like humans, flies track complex visual features that are invisible to the canonical elementary motion detector. We devised a novel white noise systems identification approach to demonstrate parallel information streams that encode diverse properties of visual features. We have also showed that flies suppress reactions to the visual surroundings to enhance tracking of a salient feature. This behavioral work has armed us with algorithms with which to make quantitative predictions for functional imaging and genetic perturbation of the visual system to probe computational mechanisms. Other labs have followed suit, expanding the research scope into higher-order motion vision in flies, which has conceptual parallels with psychophysical work in humans.

### 3.3.1 The STAF as a characterization of behavioral responses to figures

In our behavioral research, we supplemented the data obtained during our initial collaboration under FA9550-09-1-0116, and produced EM and FM STAFs for an expanded sample size. As previously described, these are based on the reaction of tethered flies (quantified by the difference in left and right wingbeat amplitude,  $\Delta WBA$ , which is proportional to turning torque) to horizontally-moving vertical bars displayed against static backgrounds in a flight arena. The EM and FM STAFs (illustrated in Figure 1 below) characterize the components of the fly's reaction induced respectively by the internal EM (if present) and by the figure itself, under an assumption of quasilinearity, including superposition of the two components in the total output. Quasilinearity is assumed to hold locally, but nonlinear variations in the STAFs can occur as figure position varies over significant ranges of azimuth. The analysis technique enables capture of these spatial variations with sets of local measurements.

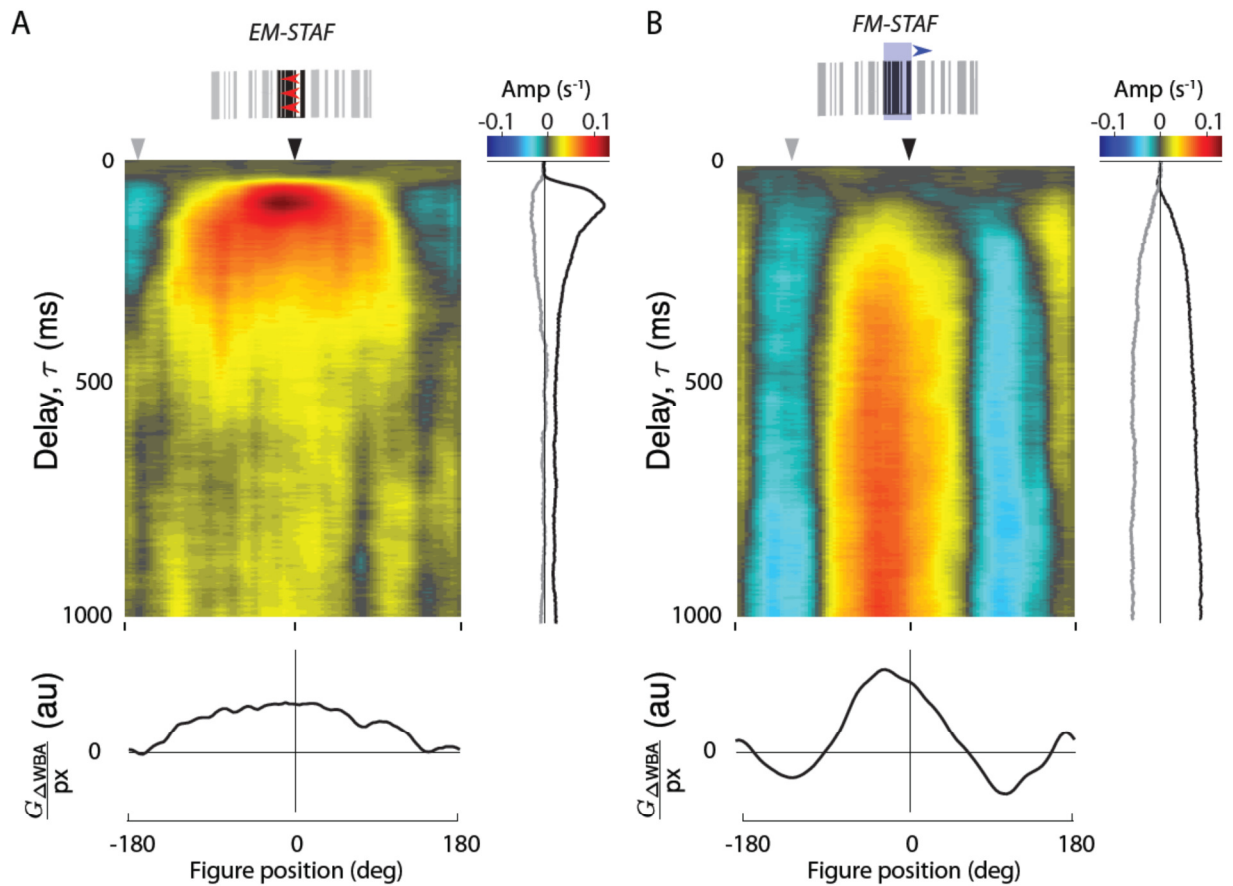


**Figure 1: Wing steering Spatio-Temporal Action Fields (STAFs) for elementary motion (left) and figure motion (right), obtained by the techniques described in the text. These respectively describe local / incremental velocity impulse responses with respect elementary motion within a figure, and motion of the figure itself, as a function of azimuthal position of the figure. The graphs to the side and below each false-color representation are cross-sections of the STAFs along the time and azimuth axes, respectively.**

In additional work, we showed that the generation of saccades, short applications of torque by an animal that in free flight cause rapid changes in direction, correlate closely with FM

STAFs (Figure 2). This strongly suggests that the subsystem that generates saccades under the experimental conditions is driven by the FM system.

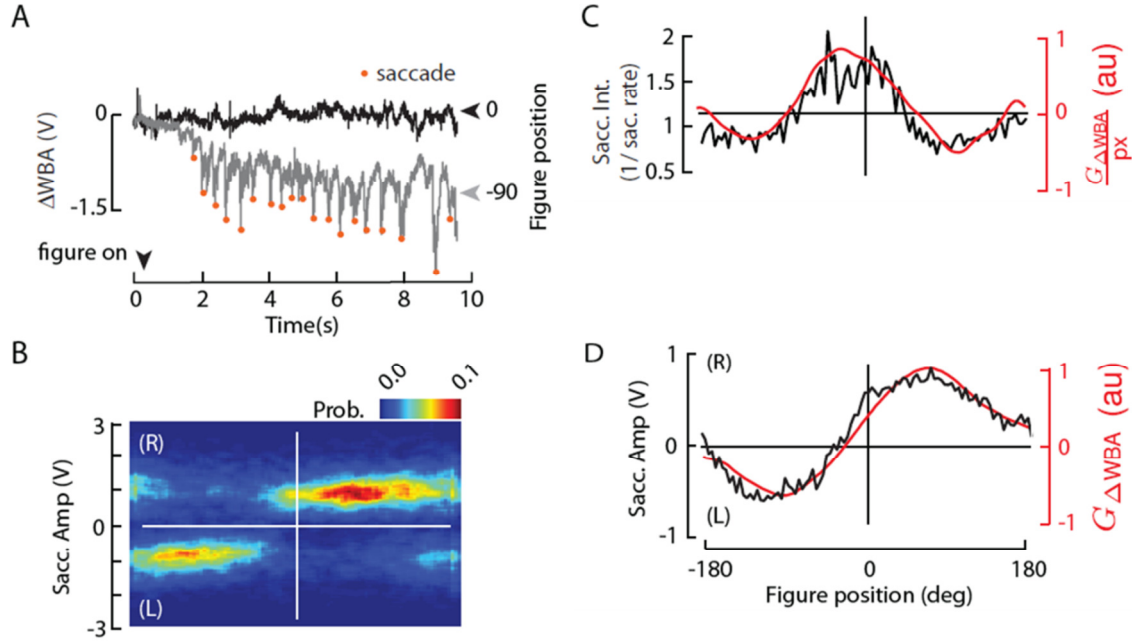


**Figure 2: Saccades are spatially mapped to the FM-STAF and enhance active visual figure tracking.** (A) Saccades evoked toward figure movement in the visual periphery, but not near visual midline. Two raw  $\Delta WBA$  traces are shown for trials in which a figure appears either in the center of the arena (black) or in the periphery (gray). Saccades are programmatically identified (orange dots). (B) Distribution of saccade amplitude under active feedback figure control. Probability distribution of saccade amplitude (uncalibrated voltage output of the wing beat analyzer, such that negative values are leftward saccades) as a function of azimuthal position of the figure. (C) Average Saccade Interval as a function of azimuthal position of the figure. Overlaid (red) is the spatial profile of the FM-STAF from Figure 2. (D) Average saccade amplitude plotted as a function of figure position (negative values are leftward saccades). Overlaid is the integral of the 'center-surround' function (red) fit to the figure STAF spatial profile, with an integration constant chosen to cause a zero crossing at 0 degrees. This function represents the amount of accumulated wing-beat difference to a figure as it is adiabatically displaced around the azimuth. For all panels,  $N=18$  flies, roughly 20,000 saccades.

Finally, in order to validate the STAF methodology, we generated predictions of the torque generated by the animals in response to stimuli other than those used to derive the STAFs, by convolving the compound EM + FM STAFs with the commanded motion. These novel stimuli included a Fourier bar, a theta bar, and a coherent motion bar with uncoupled internal and figure displacements (i.e., the same class of stimulus used for STAF derivation, but driven by a novel pair of m-sequences). We also computed predictions based on the EM and FM STAFs alone, and compared all to measured data for the same motion when displayed to a sample of tethered flies. The results are summarized in Figure 3:

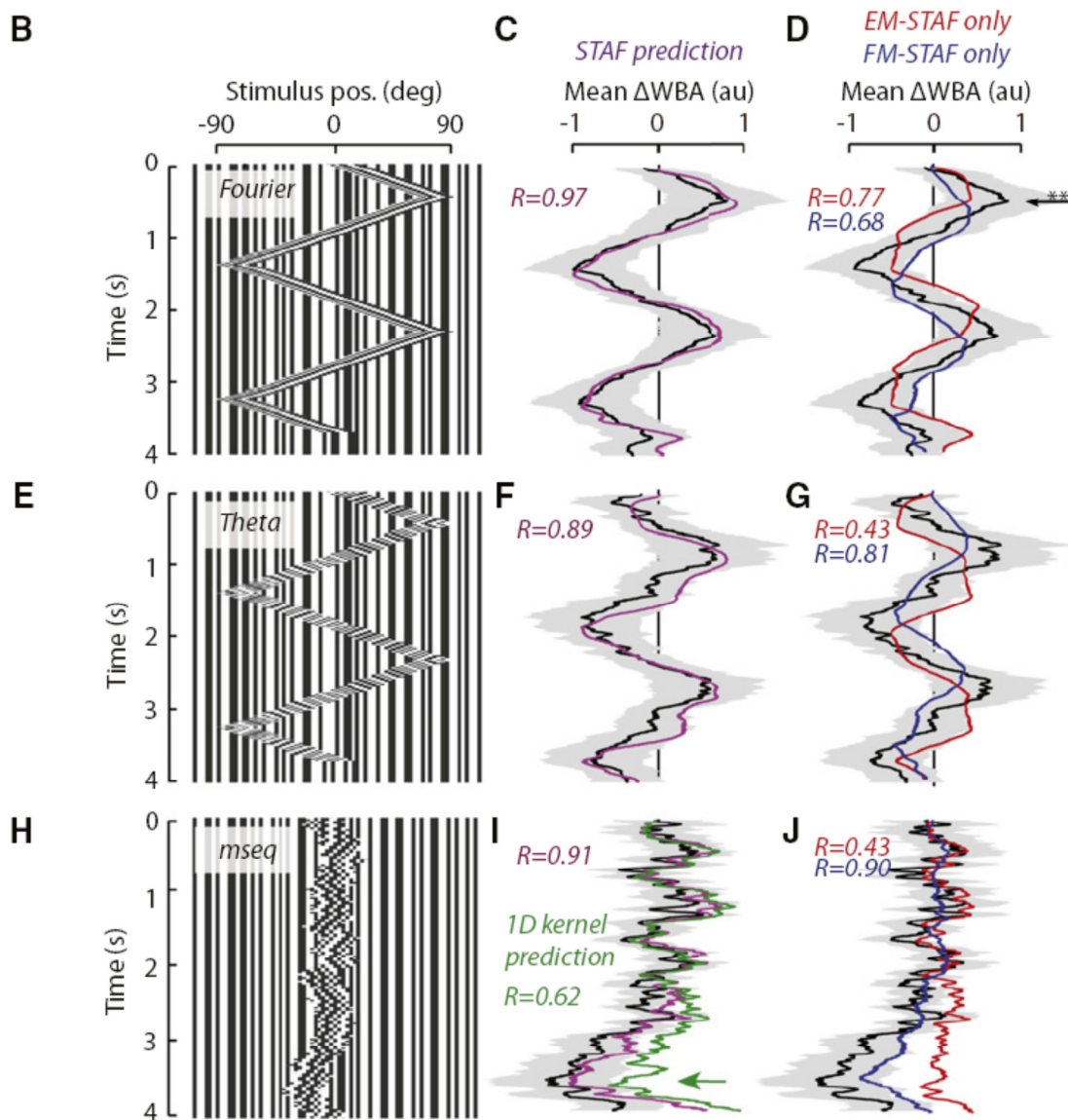
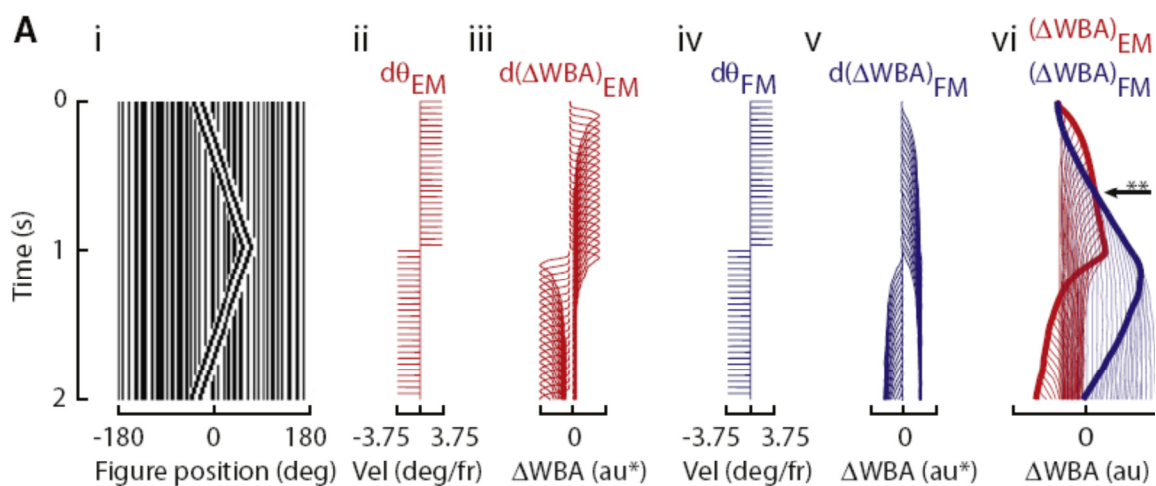


**Figure 3: (See prior page.) Convolution of complex figure stimuli with both STAFs together is sufficient and necessary to accurately predict fly behavioral responses. For all panels, N=5 flies, each having completed 96 trials. Simulations are averages of 96 trials. (A) An illustration of the incremental construction of the open loop simulation trajectory to a Fourier bar. Space-time plot (i) of the stimulus. EM system inputs (ii) and impulse responses (iii). FM system inputs (iv) and step responses (v). Composite responses attributed to each subsystem (vi) (FM, blue; EM, red) plotted after each frame (transparent) and overall. The arrow labeled \*\* indicates the time at which the FM and EM responses are approximately equal in amplitude. (B) Space-time graph indicating time variation of a single row of arena pixels. For the Fourier figure, internal elementary motion and figure position vary according to the same triangle wave with a relative gain of 1. (C) Mean behavioral responses (*black* line indicates mean fly response, *grey* envelope indicates one S.E.M.). Stimuli were convolved with each STAF, added together (*magenta*). (D) Tracking trajectories predicted by convolution with either STAF independently. Overlaid are mean behavioral responses as plotted in B. (E) Space-time graph indicating a Theta figure, for which internal elementary motion and figure position are inversely coupled with a relative gain of -1. (F) Superposed STAF prediction, plotted as in B. (G) Individual STAF predictions, plotted as in C. (H) Space-time graph, plotted as in E for a decoupled Theta bar modulated by independent m-sequences (see Fig. 1). (I) STAFs predict figure tracking responses to white noise modulated motion, plotted as in B (*black* line indicates mean fly response, *grey* envelope indicates one S.E.M.). Steering response predicted with filter kernels collected only at visual midline is indicated in *green*. As the figure diverges into the periphery, the one-dimensional kernel prediction fails (*green arrow*). (J) Individual STAF predictions, as plotted in D. For all panels, *R* value indicates Pearson product-moment correlation coefficient between mean fly responses ( $\Delta$ WBA) and STAF predictions for each visual stimulus as indicated.**

The predictive power of the compound STAF is clear in these experiments and analyses, confirming its validity as a representation of the optomotor response of tethered flies to general figure motion (for the step sizes used in the experiments).

### 3.3.2 Filters for visual figure-ground discrimination

Building upon our previous findings of independent processing streams underlying figure tracking in flies, we turned our attention to how figure tracking operates within the context of wide-field background signals generated by self-motion. We aimed to characterize the spatiotemporal properties of optomotor responses to both wide-field ground motion and figure motion for varying azimuthal positions of the figure. Adapting our previous white-noise methodology, we computing velocity impulse response filters to figure motion *and* ground motion parameterized over the visual azimuth, and generated STAFs for each. These STAFs demonstrate how the temporal dynamics of incremental steering responses to velocity impulses of a small visual figure and simultaneous velocity impulses of the wide-field ground vary as a function of the spatial location of figure motion on the visual azimuth.

We first demonstrated that flies can actively target visual figures under closed-loop feedback control even under the limit in which any incremental motion was matched by ground motion oriented in the opposite direction. Figure tracking is so robust that is impervious to wide-field motion signals that move completely out of phase with the fly's own steering commands. This can only be achieved by some mechanism of inhibition or suppression of wide-field stabilization reflexes. By using m-sequences to characterize the spatial and temporal dynamics of figure and ground motion (graphically represented by the STAFs), we show functionally how this is accomplished. In particular, we show that for figures defined only by their relative motion, (1) flies actively fixate a visual figure against a moving ground even when the motion signals



directly oppose, (2) figure and ground STAFs collected simultaneously indicate distinct spatial tuning and dynamics (Figure 4), (3) the presence of a figure is required for active suppression of the wide-field optomotor stability response (Figure 4), (4) STAFs predict fly responses to compound figure-ground stimuli. This work has been published in the Journal of Experimental Biology [2].

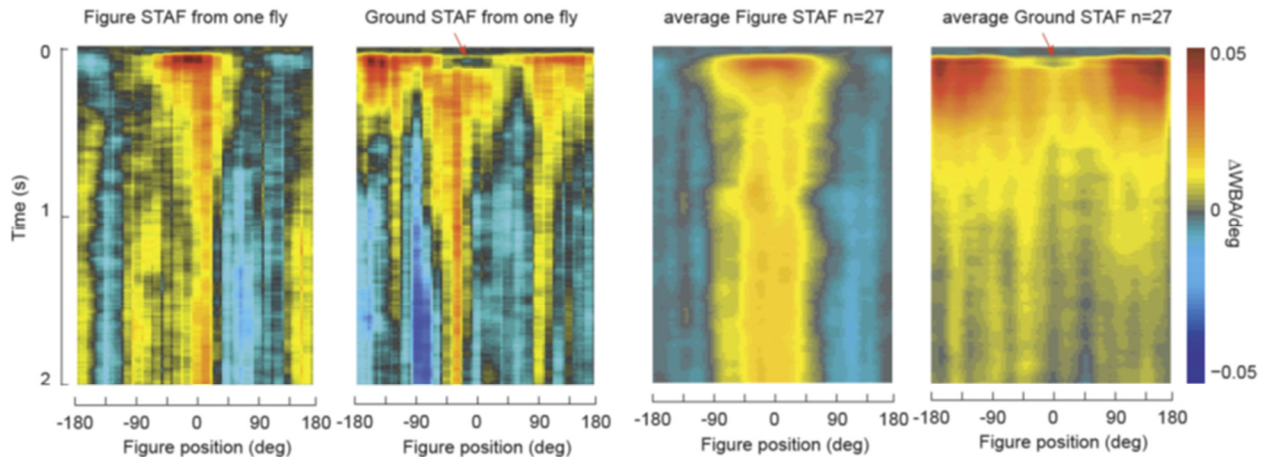


**Figure 4: Wing steering Spatio-Temporal Action Fields (STAFs) collected from a single fly, and average STAFs collected from a group of flies. STAFs reveal the robust figure tracking response on visual midline and the spatial inhibition apparent in ground responses within the region of strongest figure sensitivity ('notch' in Ground STAFs below red arrowheads). We show direct evidence of inhibition of the ground stabilization system when a figure is occupying the forward field of view, and is being actively tracked; in control experiments, replacing the uncorrelated figure motion stimulus with a figure-sized patch of uniform gray does not provoke the spatial inhibition seen here.  $\Delta WBA$  refers to the difference in wing beat amplitude across the left and right wings (units of uncalibrated sensor voltage).**

If flies suppress optomotor steering responses to wide-field motion while tracking visual figures, does that mean that they are generally unable to stabilize their visual gaze? Virtually all reports that record wing kinematics and head motions together demonstrate that the two are tightly correlated [16][48]. Yet, none investigate how the visual gaze (head orientation) is controlled during figure-ground discrimination. We used real-time tracking video to construct linear filters representing head movements in response to m-sequence-mediated velocity impulses of figure and ground motion, under similar conditions as described above. The results were surprising and informative. We note first that under identical conditions, wing kinematics share the overall control effort to simultaneously steer toward a salient visual figure and also stabilize perturbations to the wide-field ground. Thus, we recover STAFs for the figure and ground motions that are distinct in space and time (Figure 4). Head kinematics do not split the control effort, but rather seem to be completely overridden by ground motion. Thus, we recover a STAF only for ground motion, but not for concomitant figure motion (Figure 5, left and center). In the absence of uncorrelated ground motion, however, the heads of flies robustly track figure motion (Figure 5, right). These results show for the first time that the control of visual gaze can be uncoupled from the control of steering torque, but only by the relative motion of visual figures on ground. These findings are elaborated in a second paper in the Journal of Experimental Biology [3].



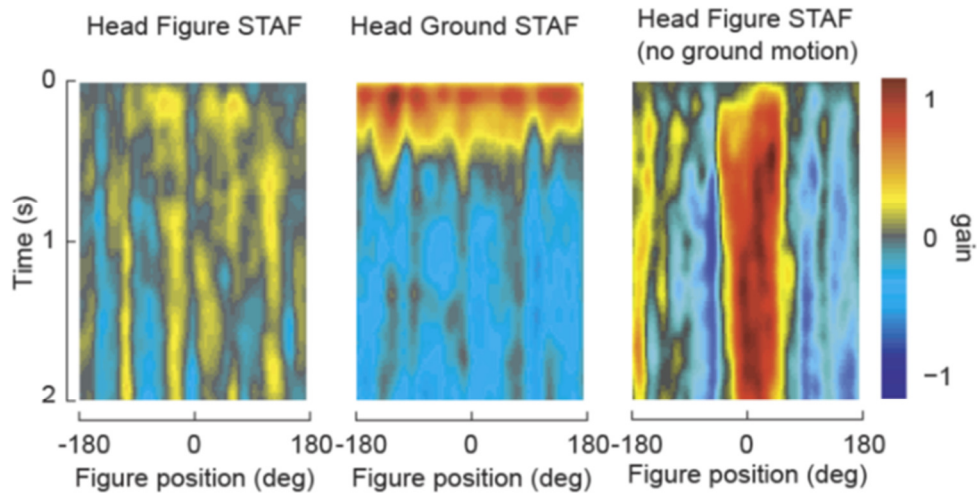


**Figure 5: Spatio-temporal action fields (STAFs) for head movements collected for  $n=27$  flies. Head STAF for figure motion (left) and for ground motion (right). Note the lack of responses to figure motion presented with concomitant ground motion (left), and the lack of any suppression of the ground response (center), even though the heads follow figure motion with there is no ground stimulus (right).**

In summary, our findings make significant headway in our understanding of simple algorithms for figure-ground discrimination, depending critically on the spatial tuning of figure tracking we reported previously [4]. Indeed the finding that figure tracking is broadly robust to head movements [4] is now extended to ground motion [3].

### 3.3.1 A figure edge is coded by the higher-order FM pathway

Tethered flies fixate a contrasting vertical bar frontally under closed-loop feedback conditions [22]. For a wide bar, fixation is bistable, with two prominent peaks in the distribution of the azimuthal position of the bar's edges, suggesting that the salient component of the figure is its edge rather than center of mass [26][34][58]. We extended those studies by using a white-noise approach to map out the underlying motion and position dependent systems that govern figure tracking [4] and measured STAFs for figures of 30 and 90 degree widths.

Comparing the STAFs reveals that the two elements of figure-tracking – Elementary Motion (EM) impulse responses and Figure Motion (FM) step responses – are affected differently by figure width (Figure 6). Consistent with a model of EM processing that relies on the summation of local motion detector inputs [23][36][50], the EM STAF broadens with figure width (Figure 6i), since more local motion detectors would be stimulated by the larger figure. In contrast, the step response of the FM STAF splits for increasing figure width (Figure 6ii, arrowheads), indicating that the strongest steering effort is produced when the edge of the 90-degree figure is aligned on midline. This supports the hypothesis that flies preferentially track the edge, or optical disparity, produced by a figure. [46]. This work is included in a manuscript currently under review at the *Journal of Neuroscience*.

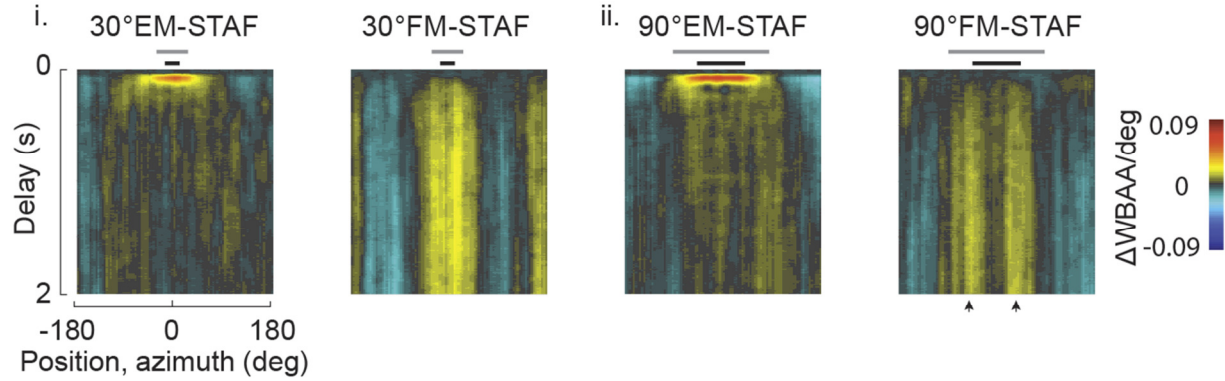


**Figure 6: Spatiotemporal action fields (STAFs) for figure motion (FM) and small-field elementary motion (EM) for a 30-degree wide (i) and 90-degree wide (ii) figure. The lobe separation for the 90-deg FM-STAF (arrowheads) corresponds to the functional separation of the two edges of the bar by the FM system.**

### 3.3.2 Figure tracking and threat avoidance by the FM system

The ability to use vision to perform a broad set of ethologically important behaviors is critical for flying insects. Importantly, the visual system must be able to robustly discriminate between visual figures that are attractive—mates, perches, food resources—and those that are aversive—predators. However, this provides a challenge to the overall system architecture of the optomotor system: to the extent that primitive visual navigation algorithms can be shared across behavioral contexts, the systems architecture can be streamlined. However, to the extent that different contexts necessitate dramatically different behaviors—fleeing a predator vs. pursuing a mate—a single, common architecture will constrain behavioral flexibility.

In this work, we employ the spatiotemporal action field (STAF) methodology to break down the fruit fly’s response to figures with different aspect ratios. We demonstrate how the existence of parallel processing streams for visual motion information that contribute in combination to the overall steering effort can accomplish a complex task, like avoidance of small objects, without wholesale dispensing with the influence of low-level programs—like EM tracking. Further, we reinforce the importance of saccadic tracking to visually-guided navigation. While saccades have long been understood as the primary navigational unit in free-flight and tethered flight where flies are allowed an axial degree of freedom, torque spikes are often neglected in rigidly-tethered flight. This study firmly identifies the saccadic tracking apparatus as the primary mechanism of small-object avoidance.

Consistent with the model of elementary motion processing being driven by a distributed set of elementary motion detectors (EMDs) likely instantiated at the level of the individual ommatidial facet, we demonstrated that the degree of EM response to small objects decreased monotonically with the vertical extent of the object. As the amount of small-field texture decreased, corresponding to a smaller overall EM motion energy, the EM response reduced correspondingly.

Consistent with the observations of Maimon et al. [35], we found that the FM-response of the fly inverts as the object is made shorter (Figure 7). This inversion takes two forms: first by the comparative reduction in amplitude of the FM STAF in the frontal visual field as compared to the rear-field, and second by the ultimate inversion of the FM STAF in the frontal visual field when the object is sufficiently short. One of the most conceptually challenging parts of the

Maimon study was the observation of small object ‘anti-fixation’ where a tethered fly under closed-loop conditions was shown to stably fixate a small-object in the rear field of view with some finite probability. This finding is consistent with the gain of the optomotor response relative to the avoided figure having a positive sign, which would allow stabilization of the figure at a particular location in the visual field. We note that the relatively unchanged and yet still-positive sign of the STAF in the rear visual field makes the rear field a comparatively more-stable pole of fixation than the frontal field, which is consistent with anti-fixation. The reduction of the STAF in the frontal field makes this frontal pole comparatively less stable and, once it actually inverts, the frontal pole becomes unstable. This demonstrates that the position-sensitive component of the fly’s steering to a small object, the FM STAF, has a distinctly different character than its EM STAF.

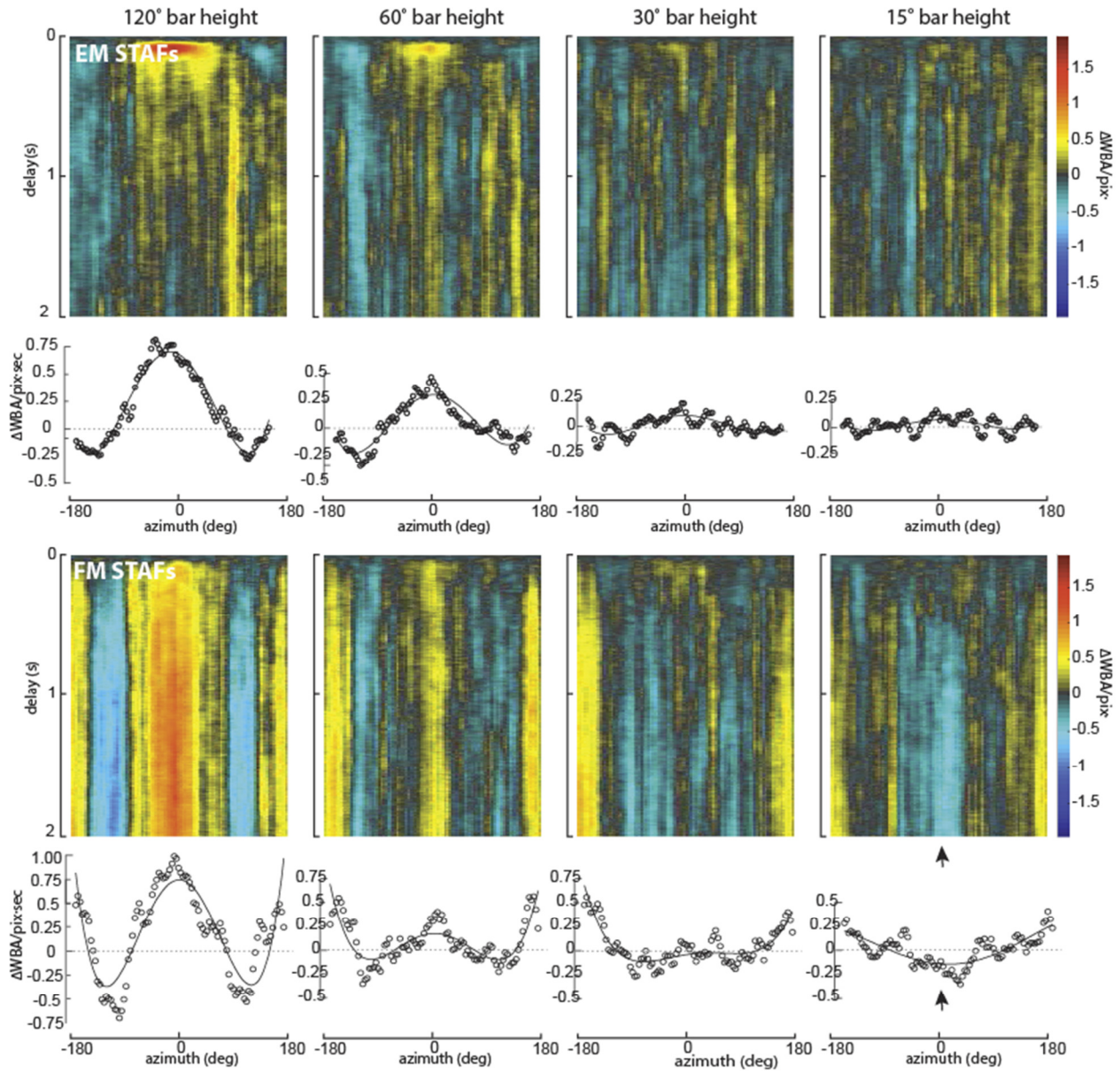


**Figure 7: Spatiotemporal action fields (STAFs) for moving bars as the bar height decreases. Below the sets of STAFs are shown their values averaged over time as a function of azimuth. These results illustrate the decrease and gradual inversion of the FM STAF in the frontal visual field, with a corresponding reduction in frontal fixation stability eventually leading to loss of the stable fixed point at front-center, and the onset of anti-fixation behavior. The EM STAF, conversely, simply decreases in amplitude as the total (first-order) motion energy decreases in proportion to bar height.**

### 3.3.3 STAFs in the frequency domain and figure tracking microsaccades

One aspect of the STAFs that limits the intuition that can be gained from them, as well as their application to engineering, is that they are measured in the time domain. It would be useful for both purposes to measure the frequency response associated with ground and figure tracking across the visual field (although care must be taken in applying frequency-domain representations to engineering and modeling, due to the inherent nonlinearities in the system).

which will become significant under large variations in figure velocities). A new postdoc in the Frye lab, Jean-Michel Mongeau, recruited from Bob Full's lab at UC Berkeley, has measured the power spectral density of time-domain STAFs (Figure 8A,B). Comparing the time and frequency domain demonstrates that when a figure is near the frontal field of view, the steering response to the figure contains higher frequency content, and correspondingly the frequency response to ground motion filters lower frequencies (Figure 8B). In addition to high frequency smooth steering toward a frontal visual figure, previous work suggested that rapid saccadic turns are oriented elicited when the figure is positioned in the visual periphery, where the azimuthal integral of the FM-STAF is maximal [4]. However, these experiments, by design, were performed on rigidly fixed flies that cannot rotate and thus cannot experience the full array of visual and mechanosensory feedback elicited during normal flight conditions. To explore the hypothesis the high frequency figure tracking and body saccades combine in active figure tracking, we used a different flight simulator apparatus in which the fly is tethered to a steel pin and suspended in a magnetic field, free to pivot in the yaw plane [6][16]. For a figure revolving at constant velocity, a fly demonstrates very clear 'microsaccades' in body orientation (Figure 8C). We have since demonstrated that flies robustly stabilize their heading between saccades (Figure 8D), and that the microsaccades are elicited near the maxima of the FM-STAF (Figure 8E,F). These microsaccades are specialized for active figure tracking, and are qualitatively and quantitatively distinct from the larger slower body saccades elicited by the visual surroundings [6]. We are currently exploring the neuronal mechanisms that trigger body saccades upon detection and discrimination of a visual figure from the moving ground.



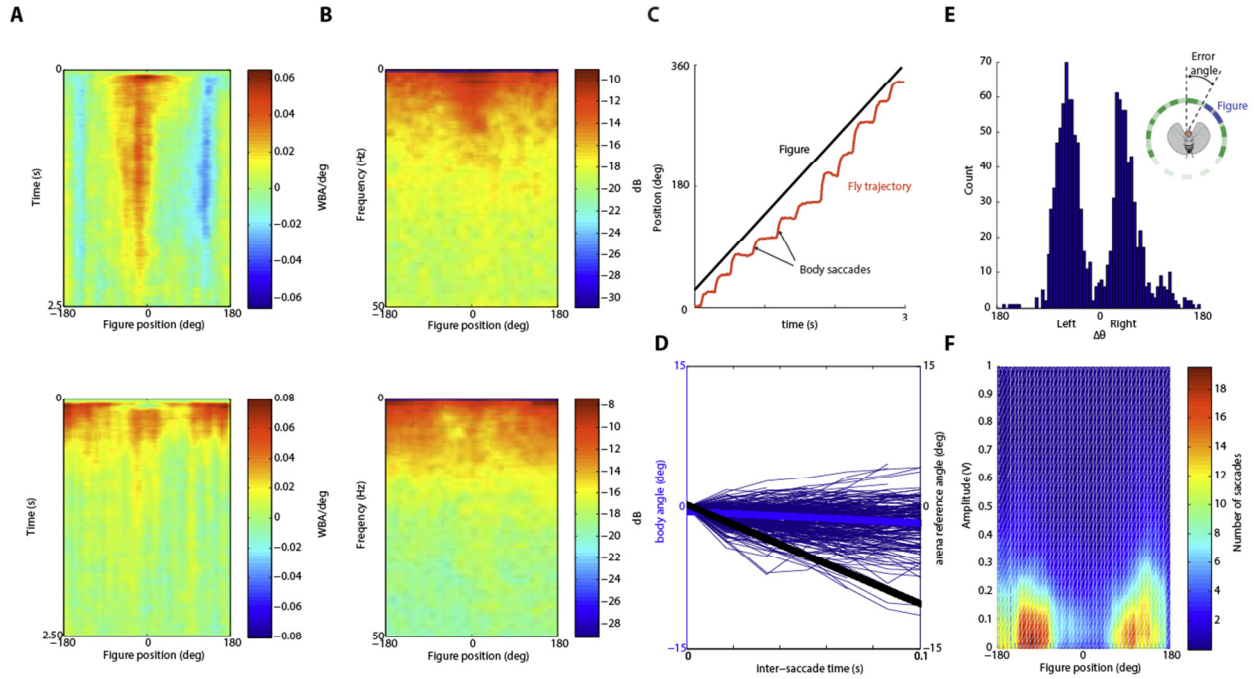


**Figure 8:** A) Time-domain figure-ground spatio-temporal active field (STAF).  $n = 14$  flies. The time-domain STAF reveals that when the figure is near the visual midline, flies track the figure, but when the figure is in the periphery, flies track the ground. B) Power spectral density of time-domain STAF. When analyzing the STAF in the frequency domain, we determined that flies' overall tracking effort is a low-pass filter in transforming the stimulus. For the figure transform, when the figure is near visual midline, flies pass higher frequencies than when the figure is in the periphery. In contrast, for the ground transform, when the figure is near the visual midline, flies pass lower frequencies when the figure is near visual midline but pass higher frequencies when the figure is in the periphery. C) Typical trajectory of a magnetically-tethered fly (red) tracking a vertical figure (black) moving on a random background. The response is dominated by body saccades. D) Inter-saccade trajectories of flies during bouts of figure tracking around the arena. Between saccades, there is little-to-no smooth tracking *via* the optomotor reflex. Thick black line is the arena reference angle. Thick blue line is the mean trajectory of flies between saccades. Thin blue lines are individual trials. E) Saccade-triggering errors between the fly's heading and the figure position. Body saccades are maximally-triggered near angles of  $\pm 90^\circ$  ( $n = 20$  flies). F) Mapping of torque spikes to figure position for figure-ground STAF experiment in rigidly-tethered flies. These results show that the highest density of torque spikes is near  $\pm 90^\circ$ , consistent with data in magnetically-tethered flies ( $n = 14$  flies).

In upcoming work, we intend to expand our understanding about figure elicited microsaccades with in vivo imaging physiology. We have begun a screen for Gal4-lines that might reasonably participate in the motor control of microsaccades in the pre-motor pathways outside of the lobula plate. In doing so, we are equipping our two-photon imaging system with a stage that allowed for imaging during tethered flight. We are also developing a computational control-theoretic model to generate specific quantitative hypotheses about the sensory information that would be expected within the control loop of figure microsaccades.

### 3.4 Electrophysiology

Our behavioral work has established that figure tracking is subserved by two parallel, superposed motion-processing streams, one coding for elementary motion (EM) cues (i.e., motion that is spatiotemporally luminance-correlated and thus directly encodable by EMDs), and the second for figure position via figure motion (FM) cues that may be higher-order in nature. In the electrophysiology element of the project we thus set out to investigate what neurons may underlie the demonstrated FM sensitivity in flies. We began with the well-known lobula plate tangential cells (LPTCs), which synapse directly with descending neurons that control the behavioral optomotor response, and whose responses to wide-field elementary motion have been widely studied (see, e.g., [8][9]). Interestingly, the LPTCs that we chose for initial investigation (belonging to the *HS* and *VS* systems) have heretofore been assumed to be wide-field integrators of EMD outputs – so any response to higher-order motion in these neurons would be of particular interest.

Recent work from the Borst group [5] also supports this general subdivision, into EM and FM processing streams. Interestingly, however, the authors suggest that the lobula plate is entirely dedicated to the computation of wide-field EM and serves no role in the detection of figure motion. This conclusion is in stark contrast with results from our own work.

#### 3.4.1 *Sensitivity to higher-order motion in the LPTCs*

To investigate the sensitivity of fly LPTCs to higher-order motion, we recorded intracellular responses in the hoverfly lobula plate. We quantified responses to moving bars, including those corresponding to ordinary moving objects (Fourier bars), but also to second-order bars in which the internal pattern dynamics did not correspond to the figure's motion. In the latter cases, the EMDs that are supposed to underlie LPTC responses are not expected to give net responses that track the figure velocity. Figure 9 depicts the stimuli used and responses of a simple EMD-based model:

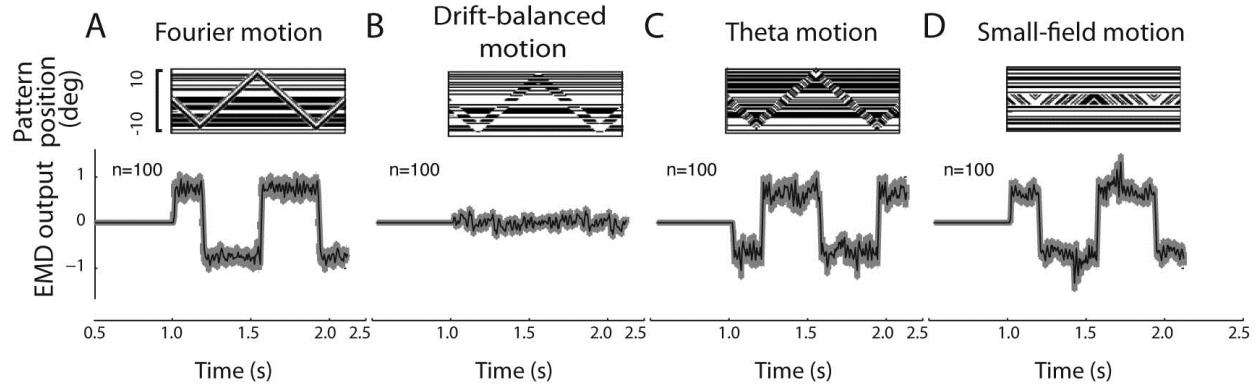


**Figure 9:** Data in column A relate to Fourier bars, column B to drift-balanced bars, column C to theta bars, and column D to small-field motion. The first row shows example space-time plots for each stimulus, where the vertically oriented bar ( $6 \times 37^\circ$ ) moved horizontally at 2 pixels per frame, corresponding to ca.  $50^\circ/\text{s}$ , for 375ms before switching direction, except in column D where the figure itself remained stationary while the internal pattern moved. In these plots, the abscissa represents time and the ordinate azimuth relative to front and center, and the displayed pattern (which is one-dimensional since it consists of uniform vertical stripes) is represented in black and white as a function of position and time. Data in the second row show the summed output in arbitrary units of a standard EMD in response to 100 randomly generated stimuli of each class. There is no net response to drift-balanced motion, whereas for theta motion, it is the internal pattern velocity rather than the figure that is followed.

Defining ‘preferred direction’ as the direction of first-order motion that produces maximum depolarization, we surprisingly found regions of high sensitivity (i.e., depolarization) in the lobula plate cell HSN when *any* type of bar moved in the preferred direction (Figure 10). For the theta bar, this means that the net neural response is *opposite* to the expected elementary motion response. (This characteristic, however, does not prevail for anti-preferred direction motion.) The FM sensitivity was particularly robust along the visual midline of the fly (shaded area, Figure 10), supporting a possible role in the behavior when bars containing higher-order motion cues are actively fixated in the frontal visual field.



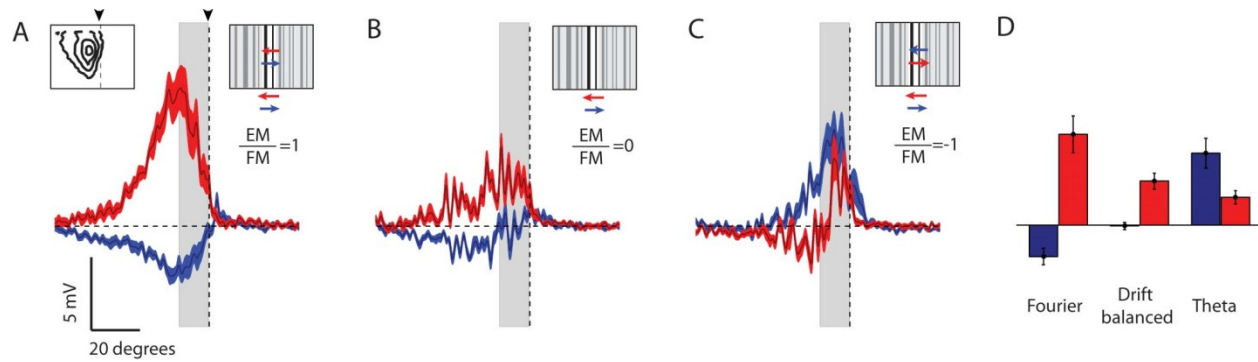


**Figure 10:** A) When a Fourier bar moves in the preferred direction (red) over a random background with the same contrast and spatial characteristics as the bar itself, the neuron responds with a depolarization that, when plotted as a function of azimuth, reflects the shape of the underlying male HSN receptive field (inset). The response to anti-preferred direction motion (blue) is inverted and weaker in amplitude, but follows the same general shape. B) In a drift-balanced bar there is no first-order motion in the internal pattern ( $EM=0$ ) as the figure sweeps across the visual field. The two data traces show the responses to preferred direction FM (red) and anti-preferred direction FM (blue). C) The two data traces show the responses to theta motion where FM is in the preferred direction (red) and anti-preferred direction (blue). D) A quantitative comparison of the mean responses to the three bars,  $10^\circ$  ipsilateral of the visual midline (shaded in A-C). Red bars show responses to preferred direction FM, blue responses to anti-preferred direction.

Interestingly, we found similar behavior in a number other HS and VS neurons: when any figure moves in a neuron's preferred direction, the neurons tend to depolarize even for drift-balanced and theta bars.

We quantified the sensitivity to pure EM (small-field motion) and to pure FM (a drift-balanced bar) across the visual field (spatial sensitivity) and time (temporal profile). This showed the FM sensitivity to be a lot more 'jagged' than the EM sensitivity (Figure 11). We found no large differences in the response onset to motion direction reversals, but in response to FM the membrane polarization builds up a lot more slowly than it does for EM. This again suggests a different underlying input behind the observed FM sensitivity in LPTCs.

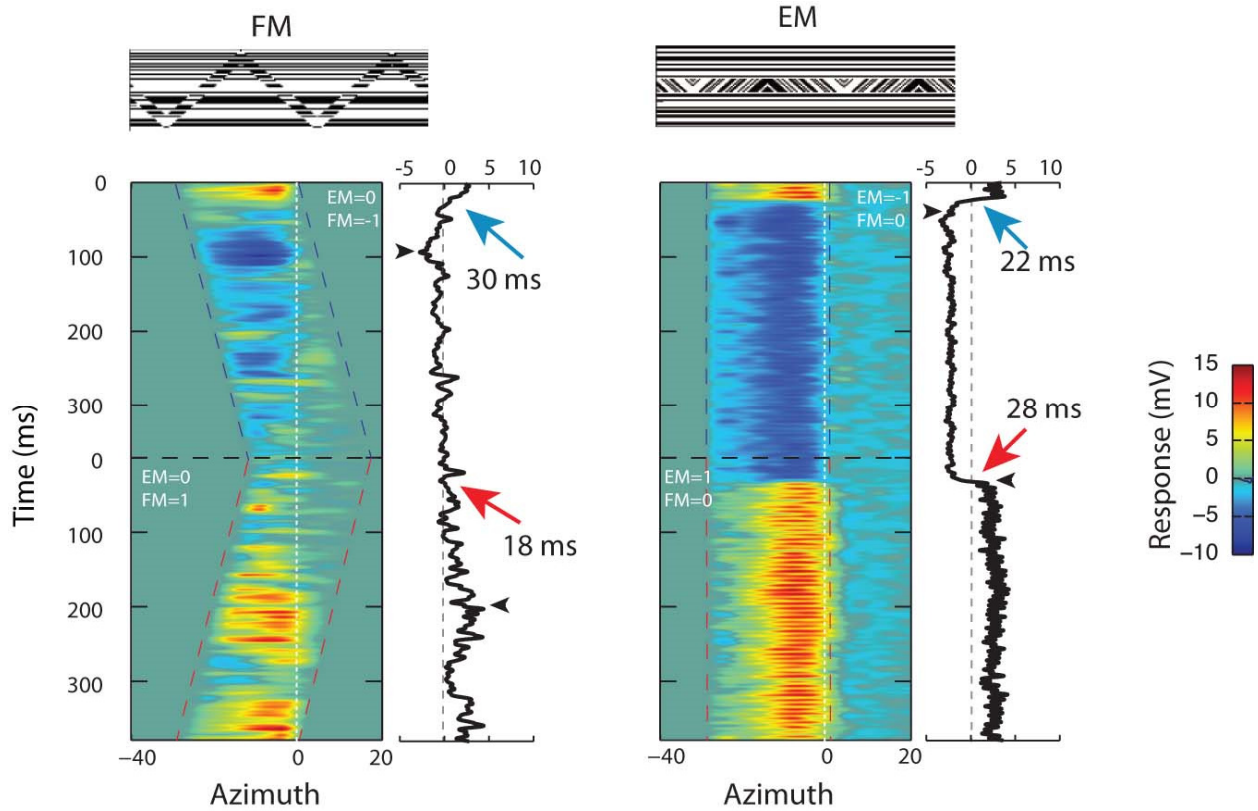


**Figure 11:** The responses to EM and FM from different parts of the visual field, displayed as a function of time since direction reversal on the y-axis, and the corresponding azimuthal location on the x-axis. The top rows show example space-time plots. Both stimuli were vertical bars ( $8 \times 75^\circ$ ). The FM bar moved horizontally at 2 pixels per frame, corresponding to ca.  $50^\circ/\text{s}$ , for 375ms before switching direction. The EM bar remained stationary while the internal pattern moved. Left column: As an FM bar moves to the right, i.e. in the anti-preferred direction of the recorded neuron, it leaves the ipsilateral visual field and moves into the contralateral visual field during its trajectory. As the bar crosses the midline (white dashed line) the membrane potential returns to pre-stimulus levels. When the bar changes direction and moves in the preferred direction of the neuron, HSN depolarizes as the bar enters the ipsilateral visual field. The blue and red dashed lines indicate the part of the visual field covered by bar motion at each point in time. To the right of each spatio-temporal response plot we show the response averaged across space, as a function of time. The red and blue arrows indicate the time at which the response changes sign after direction reversal. The time-to-peak response is longer for FM than for EM: 90ms and 190ms for FM (arrowheads), and 33ms and 30ms for EM.

These findings were published in the Proceedings of the National Academy of Sciences [32], with key points are highlighted above.

### 3.4.2 Figure-ground discrimination in hoverfly LPTCs

In this project we have shown that figure-ground behavior can be broken down into separate components that code for the motion of the background, the elementary motion associated with the bar and the position of the bar, respectively, as described in detail above. Interestingly, previous work has shown that local features have a strong influence on the response properties of HS cells. For example, during optic flow reconstructed from actual flight paths, the translation of

near-by features generates strong transient responses in blowfly HS neurons [7][31][33]. In hoverfly HS neurons, high-contrast, vertically oriented features generate strong contrast gain reduction that reduces the response to subsequent low-contrast stimuli [41]. Furthermore, pattern noise, i.e. the response to individual features within a scene, is stronger in hoverfly HSN, with its small receptive field, than in HSNE [42], which has a more LPTC-typical, laterally extended receptive field [38]. Particularly the HSN response to vertically elongated features is enhanced, suggesting that it may be involved in forward fixation behaviors [42].

To further investigate responses to figure motion in the LPTCs, we recorded intracellular HS responses to salient bars moving with or against a broadband background moving at the same velocity, and compared the responses to bar and background motion on their own. The bars were narrower than the acceptance angle of a single ommatidium, ensuring that the background motion constitutes the spatially dominating component of the visual stimulus. When moving in the preferred direction over a mean luminance background, the bar generates a strong depolarization of male HSN (black, Figure 12A), and a hyperpolarization in the anti-preferred direction (black, Figure 12B).

The broad-band background image (for description, see [39]) also drives the neuron strongly in both the preferred and anti-preferred direction (grey data, Figure 12). Despite the bar's narrow spatial extent, it generates a stronger response than the background when it moves through the HSN receptive field (compare black and grey responses, Figure 12), suggesting strong neural amplification of the response to the bar.

We examined bar-background responses by displaying the bar over the background. When the background moves in the preferred direction, and the bar passes through the receptive field in the preferred direction (red, Figure 12A), the response shape resembles the bar response (black, Figure 12A) more than the background response (grey, Figure 12A). When the background moves in the opposite direction to the bar, the response also largely resembles the bar response (compare black and blue, Figure 12A). Indeed, when the bar moves through the receptive field, HSN is strongly depolarized (blue, Figure 12A), despite 99% of the visual stimulus moving in its anti-preferred direction. The strong correlation with the bar response is particularly evident in the 400ms surrounding the receptive field hot-spot (Figure 12C).

When the bar moves in the neuron's anti-preferred direction, the response to bar-background motion also resembles the response to bar motion (black, Figure 12B) more than the response to background motion (grey, Figure 12B), if the background moves in the anti-preferred direction (cyan, Figure 12B). However, when both the background moves in the preferred direction (green, Figure 12B) the response does not reach the same level of hyperpolarization as during bar motion alone (black, Figure 12B).

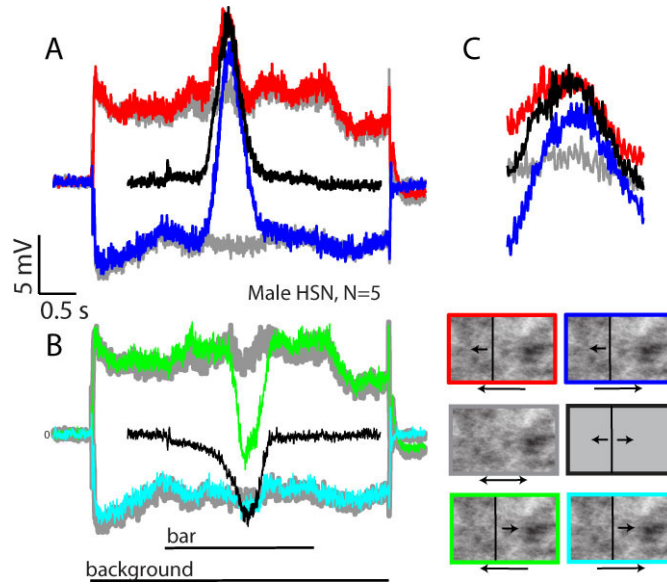


**Figure 12: HSN background responses to figure-ground motion. A.** The response of male HSN to a black bar moving in the preferred direction over a mean-luminance background (black,  $N=5$ ). The grey data show the responses to the background pattern moving in the preferred or anti-preferred direction. The red data show the response when the bar and the background both move in the preferred direction, with no velocity difference. The blue data show the response to the bar moving in the preferred direction over the background moving in the anti-preferred direction. **B.** The male HSN response to bar motion in the anti-preferred direction (black). The cyan data show the response to both bar and background moving in the anti-preferred direction and the green data the response to the bar moving in the anti-preferred direction over the background moving in the preferred direction. The bars under the trace show the peri-stimulus durations for bar and background motion. The data were low-pass filtered for display. **C.** A magnification of the data in panel A for the 400ms used for quantitative analysis in subsequent figures. The frames of the pictograms are color coded to illustrate the four combinations (red:  $\text{bar}_{\text{pref}}\text{-background}_{\text{pref}}$ , blue:  $\text{bar}_{\text{pref}}\text{-background}_{\text{anti-pref}}$ , green:  $\text{bar}_{\text{anti-pref}}\text{-background}_{\text{pref}}$ , cyan  $\text{bar}_{\text{anti-pref}}\text{-background}_{\text{anti-pref}}$ ).

To quantify these results, we display the response to bar-background motion as a function of the response to bar motion alone, during the 400ms the bar passed the receptive field center (as magnified in Figure 12C). This analysis shows a strong correlation between the bar-background response and the bar response (Figure 13A, D; the data are color coded to illustrate the four conditions), and only a poor correlation with the background response (Figure 13B, D). To test whether the response to bar-background motion represents a summation of the individual responses to bar motion and background motion, respectively, we display the response to bar-background motion as a function of the sums of the responses to bar motion alone and background motion alone (Figure 13C, D). This analysis suggests that the linear sum of the responses to bar motion and background motion, respectively, only gives a good correlation with the bar-background response when the background moves in the preferred direction and the bar

in the anti-preferred direction (green, Figure 13C, D). In all other cases, the response to bar-background motion is most similar to the response to bar motion alone (black data, Figure 13D). This suggests that the bar response dominates in compound responses to bar-background motion.

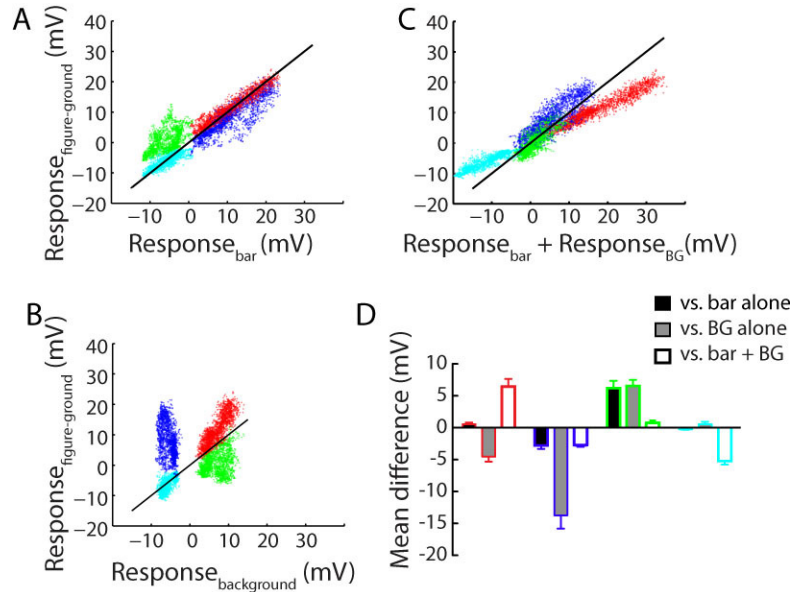


**Figure 13: HSN background responses are suppressed by motion of a salient bar. A.** The response to figure-ground motion as a function of the response to bar motion alone, for the 400ms surrounding the receptive field center. The data points are color coded according to the pictograms and data in Figure 12B. The response to figure-ground motion as a function of the response to background motion. C. The response to figure-ground motion as a function of the summed responses to bar motion and to background motion on their own. D. The difference of the mean response (in mV) between the response to figure-ground motion and bar motion alone (black fills), background motion alone (BG, grey fills), and the sum of background and bar motion responses (white fills). The frames of the bars are color coded to illustrate the four combinations of motion directions.

Among LPTCs, the hoverfly HSN neuron stands out with its unique receptive field, with a high gain, particularly close to the visual midline [38]. It is possible that the uniquely high gain might explain the strong response correlation with the motion of a salient bar. To test this, we record the response to the same set of stimuli in HS neurons with broader receptive fields. To summarize the comparison we measure the absolute mean difference during the 400ms the bar passes the center of the receptive field. We use the absolute difference to avoid averaging out positive and negative differences, as in the red ( $\text{background}_{\text{pref}}$ ,  $\text{bar}_{\text{pref}}$ ) and the green data ( $\text{background}_{\text{pref}}$ ,  $\text{bar}_{\text{anti-pref}}$ ).

We found that male HSN responses to our bar-background stimuli are more similar to bar motion alone (black, Figure 14), than to background motion alone (grey, Figure 14), or to the sum of the responses to the individual stimuli (white, Figure 14).

Even if bigger than the male HSN receptive field, the female HSN also has a small receptive field, sharply delineated at the mid-line [38]. In female HSN bar-background responses are also

more similar to bar motion alone (black, Figure 14), than to background motion alone (grey, Figure 14), or to the sum of the responses to the individual stimuli (white, Figure 14).

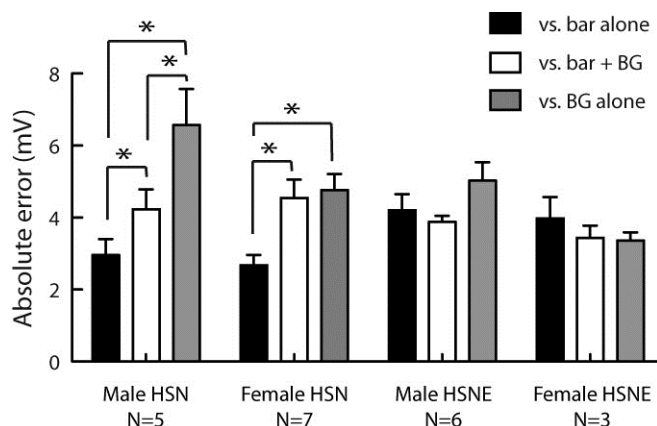


**Figure 14: The high correlation with bar responses is unique to HSN. Comparison between the responses to figure-ground motion, and the responses to bar motion alone (black), background motion alone (grey), or the sum of the responses to bar and background motion, respectively (white). The data show the absolute mean difference for the four combinations of bar and background motion shown in Figure 13. Stars (\*) indicate significant difference ( $p < 0.05$ , paired t-tests) between errors.**

However, in male and female HSNE, with a more LPTC-typical, laterally extended receptive field, the response to our bar-background stimuli are equally similar to the responses to bar motion alone (black, Figure 14), background motion alone (grey, Figure 14), and the sum of the responses to the individual stimuli (white, Figure 14). This suggests that the strong correlation we see between bar-background motion and bar motion in HSN, has to do with the unique receptive field properties of the most dorsal HS neuron in hoverflies, rather than be ubiquitous feature for LPTCs. This is supported by previous work showing a high gain particularly to vertically extended, salient features, in hoverfly HSN [41][42].

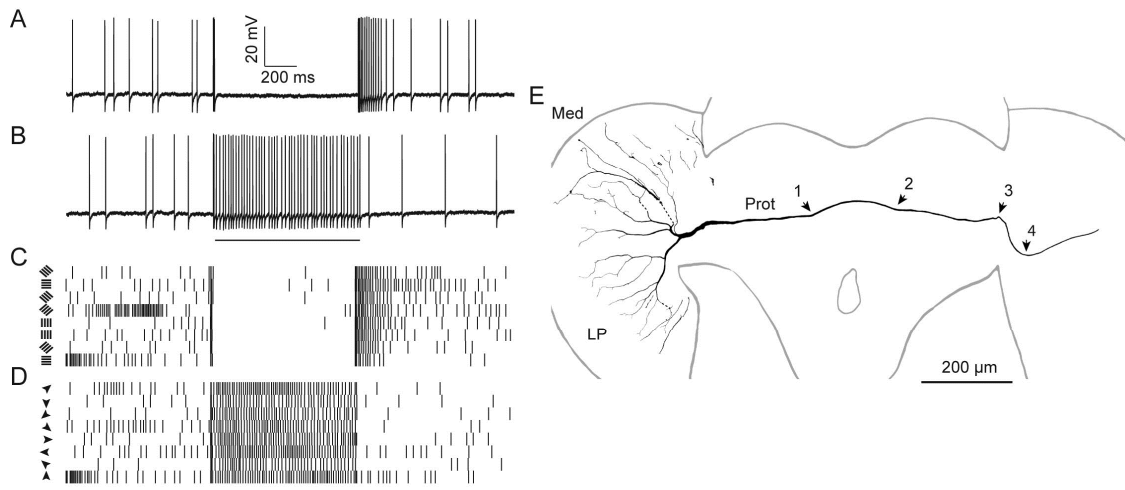
Some of these findings have been included in a paper that has been resubmitted to the journal *PLoS One*, and the remainder will be covered in a manuscript that is presently in production.

### 3.4.3 Centrifugal stationary inhibited flicker excited (cSIFE) Neuron

During the second year of the project we published a paper providing further support for non-EMD type input to the fly lobula plate. The cSIFE (centrifugal stationary inhibited flicker excited) neuron has extremely intriguing physiological response properties. It responds with a low but finite spike rate to a visual stimulus with no spatial contrast, but if a high-contrast, stationary pattern appears on the screen, it gives one or two transient spikes followed by pronounced inhibition of the spike rate (Figure 15A, C). In contrast, the cell is excited – i.e. displays significant increase in spike rate over the no-contrast case – if the pattern moves (Figure 15B, D) or flickers. During the third year, we continued characterization of cSIFE.

In our Year 2 work, we found that cSIFE was strongly excited by flicker, up to high temporal frequencies, with ON and OFF contrast changes coded independently. The flicker sensitivity leads to responses to stimuli moving in any direction (Figure 15D). Importantly, however, the strong inhibition of cSIFE by stationary sinusoidal gratings of any orientation (Figure 15C) is unlike flicker-sensitive neurons described in earlier visual pathways [43]. cSIFE could thereby serve as a neural substrate for the coding of stationary stimuli, as well as of high-frequency flicker, such as might be associated with sudden perturbations from visual stability.

cSIFE is a heterolateral neuron with output dendrites covering the expanse of the lobula plate (Figure 15E). These outputs affect the response properties of neurons sensitive to optic flow [15], and cSIFE may thereby play a profound but hitherto unappreciated role in the coding of vision. Despite having its output dendrites in the lobula plate (Figure 15E), it clearly does not derive its sensitivity from underlying EMDs. This thus provides even stronger evidence for non-EMD type input to the lobula plate [13].



6

**Figure 15: Centrifugal stationary inhibited flicker excited, a novel lobula plate neuron.** A. Neural response to a stationary sinusoidal grating (0.1 cycles/degree) presented for 1s. B. Neural response to a moving sinusoidal grating (0.1 cycles/degree, 5Hz). The bar under the raw data indicates the stimulus duration for panels A and B. C. Raster plots where each vertical line indicates the timing of an action potential. The second to last row represents the data shown in panel A. The data in each row show the response to a stationary grating (0.1 cycles/degree) of different orientation, as indicated by the pictograms to the left. D. Raster plots of responses to sinusoidal gratings (0.1 cycles/degree, 5 Hz) moving in different directions, as indicated by the arrowheads to the left. The second row from the top represents the data shown in panel B. E. Morphology of cSIFE. The neuron was recorded and filled in the left lobula plate. Arrowheads 1 and 2 indicate a posterior dip of the main axon, as do arrowheads 3 and 4. Med = medulla, LP = lobula plate, Prot = protocerebrum.

cSIFE's inhibition by spontaneous patterns does not depend on pattern orientation (Figure 15C), and neither does the excitation depend on the direction of motion (Figure 15D). Since



cSIFE's response to motion is non-directional, whereas directionality is a key feature of EMD-type input, we went on to study its dependence on pattern wavelength. We found that the excitation increased with pattern wavelength (Figure 17A), also arguing against an underlying EMD-type input.

When using higher temporal frequencies the response continued to increase with no clear peak. This prompted us to use a sinusoidal flicker, and indeed, the response was stronger than to motion (Figure 16, green). This further supports the notion that the cSIFE response that we recorded to motion is derived from a high sensitivity to flicker, and not to elementary motion.

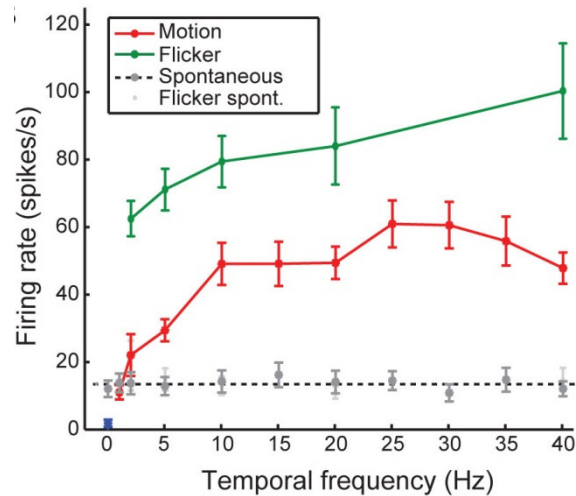


**Figure 16: cSIFE's motion response is flicker derived.** The response of cSIFE as a function of temporal frequency of a full-screen, full-contrast sinusoidal grating (0.1 cycles/degree, red, N=11). The red data show the response to motion, and the green to full-screen, sinusoidal flicker at a subset of these frequencies (N=8, except at 2 and 40 Hz where N=6).

Finally, cSIFE inhibition by stationary patterns is limited to a narrow band of wavelengths (ca. 0.08-1 degrees). When displaying patterns with wavelengths above or below this cut-off, we saw no inhibition below spontaneous rates (grey, Figure 17A).



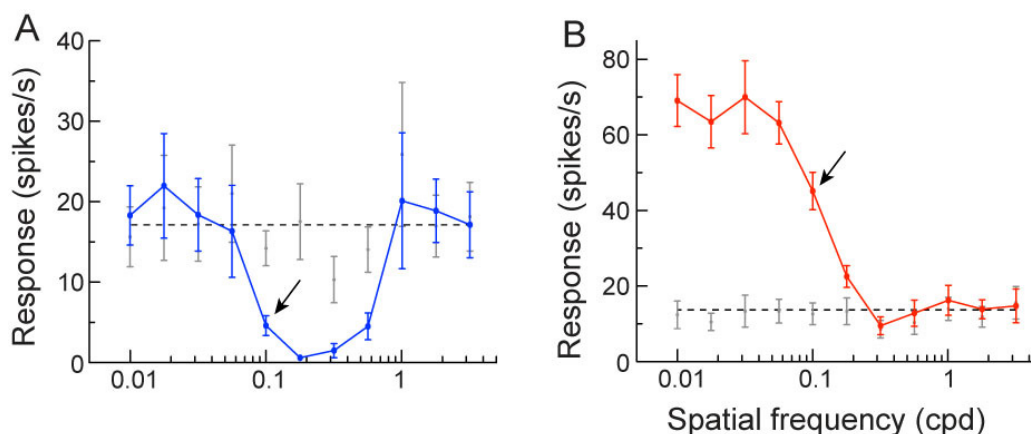


**Figure 17: Spatial frequency sensitivity. A.** The response of cSIFE as a function of spatial frequency of a stationary full-screen, full-contrast sinusoidal grating (N=8). **B.** The response of cSIFE as a function of spatial frequency of a full-screen, full-contrast sinusoidal grating moving at 5 Hz. N=10.

These findings were published in Journal of Neuroscience [15], with some key points reproduced here.

During the final year of the project, we investigated the responses of cSIFE to natural images. These were presented either as stationary (to induce inhibition), or moving (to induce excitation). Here we present the inhibition experiments. We chose five HDR images taken from natural hoverfly habitats [11], and the broadband image used in the experiments above (Figure 12). The images (Figure 18) cover a range of contrasts and contain differences in their distribution of features.

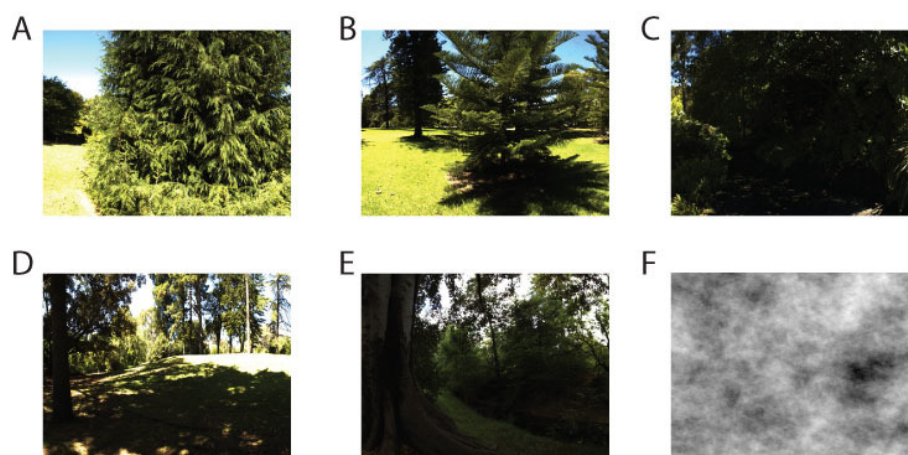


**Figure 18: The naturalistic images used in the cSIFE experiments. Images A-E** come from a database of HDR images obtained by Brinkworth and O'Carroll from natural hoverfly habitats. **Image F** has been used in several publications, including the study described above (Figure 12).

We found that all 6 images inhibited the spontaneous rate of cSIFE, but that the inhibition by the different images varied (Figure 19), and in no case was the inhibition as strong as when using single frequency sinusoidal gratings (Figure 17).

To investigate this in more detail, we plot the same data, but use the image contrast on the x-axis. This analysis shows that there is a clear correlation between image contrast and the strength of the inhibition. This compares well with our findings from our *Journal of Neuroscience* paper (using sinusoidal gratings).

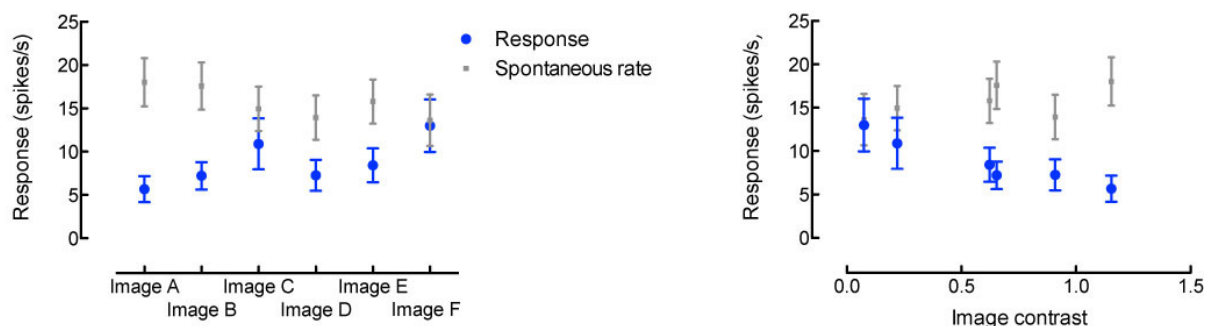


**Figure 19: Inhibition of cSIFE’s spontaneous rate by different natural images (N=16).** The plot on the left show the images organized as described in Figure 18 above. The plot on the right shows the inhibition by the different images when these are organized after their respective contrast.

As of the close of the project, we were conducting experiments in which the contrast of two of the images (A and D) was manipulated to determine how that affects the inhibition. Results have now been submitted to *Nature* communications and are presently under review.

### 3.5 In-Vivo Imaging

During the final reporting period, we used two-photon excitation calcium imaging in conjunction with genetic techniques to target and examine feature detection by specific cell types *in vivo* to various types of figure and edge-related stimuli. We survey four cell types that project from the fly lobula – a proposed feature selective region, and an attractive target for study due to the paucity of physiological work that has been done there – and which terminate within discrete optic glomeruli in the central brain. We find that the physiological responses of each cell type encode different features of figure-ground stimuli, composing a hierarchy of figure-like percepts. Two of the cell types we probed, termed LC12 and LC10a, (Figure 20) – both having projections that pass through the Anterior Optic Tract (AOT) – specifically encode sufficient information to discriminate a small moving figure on a moving ground, while showing homologous responses across the space of figure-like stimuli that elicit similar behavioral responses. In brief, we take advantage of a yeast transcription factor, Gal4, which labels select subsets of neurons. We use Gal4 to “drive” the expression of any gene of choice, such as green fluorescent protein (GFP) for anatomical identification, or GCaMP for *in vivo* calcium imaging.

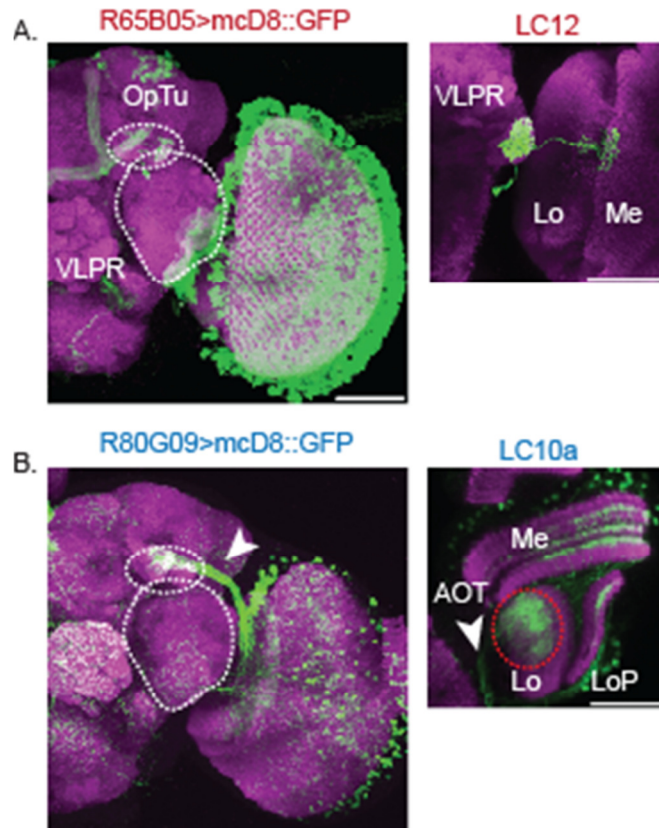


**Figure 20: Anatomy of two example lobula glomerular projection cell systems.** Indicated are images of the right brain hemisphere with prominent optic lobes, lobula (Lo), medulla (Me) and the ventrolateral protocerebrum of the central brain (VLPR). (A) GFP staining (green) of a Gal4 line (R65B05) labeling the identified LC12 columnar neuron in the lobula (Lo). Inset shows a single cell clone isolated from the full expression profile, indicating dendrites within the outer layer of the lobula (near the lower medulla), with an axon projecting into a glomerulus of the ventrolateral protocerebrum (VLPR). (B) The full Gal4 expression profile of LC10a columnar cell (R80G09 Gal4 line) that projects through the anterior optic tract (AOT) into the optic tubercle (OpTu). Note that the LC10a line labels extraneous neurons of the medulla and lobula plate, but imaging was restricted to the lobula, where only this cell class is labeled by the Gal4 driver.

The four anatomically identifiable cell-types that we selected for study are distinguishable from one another by each having a projection pattern to a distinct optic glomerulus [51][44] or the lobula plate [30]. Two of these are shown here for example (Figure 14). The lobula is the most distal area of the optic lobe where retinopic inputs are broadly recombined and outputs projected into glomeruli, in a convergent architecture similar to that seen in the antenna lobe. This anatomical convergence suggests that the lobula forms a nexus between sensation and abstract feature coding [52][53]. LC12 is a columnar-type neuron that projects to the lateral portion of the ventrolateral protocerebrum (VLPR). LC10 is columnar-type neuron that projects through the Anterior Optic Tract (AOT) to the anterior portion of the optic tubercle (optu). These two cell classes, plus the two others not shown, were probed *in vivo* with a suite of figure and edge stimuli; results from such experiments on LC12 and LC10a are depicted below in Figure 21:

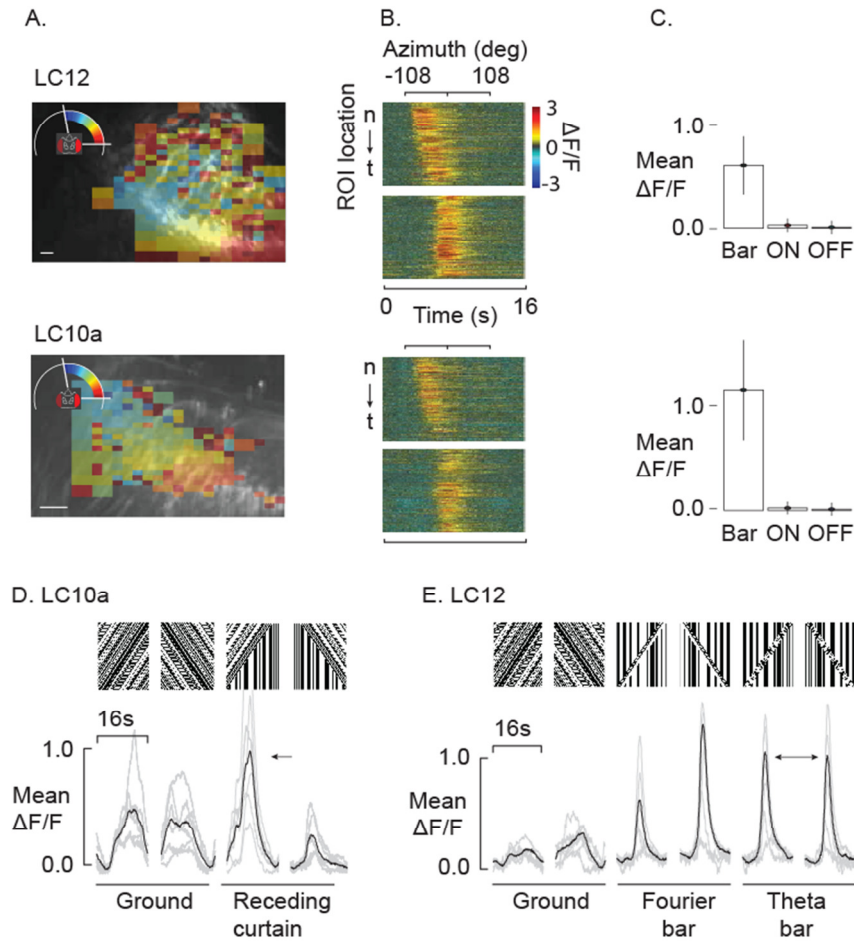


**Figure 21: Calcium responses from lobula projection neurons imaged with genetically encoded fluorescent calcium reporter GCaMP6.** A live fly is restrained under the objective of a two-photon scanning laser excitation microscope, viewing a LED display identical to those used in the behavioral experiments. A small window is cut in the rear of the head capsule to view the Gal4-GCaMP labeling within identified neurons of the lobula. (A) A full-field image of many individual columnar LC12 neuron dendrites within the lobula. False color is added to indicate the retinotopic receptive field of the dendrites. (B) Excitatory calcium responses from multiple regions of interest (ROIs) ordered from the nasal (n) to temporal (t) direction. Upper graph shows the fluorescence response to a 30-degree Fourier bar sweeping across the LED display. Note the timing offset generated by the sequential activation of ROIs at each retinotopic position. We observed no heterogeneity in the responses, so we time-shifted the response and pooled them (lower inset panel). (C) Mean  $\Delta F/F$  responses to bar motion compared to switching the arena ON and OFF. (D, E) Exemplar responses of LC10a and LC12 to complex figure-ground stimuli. Insets represent space-time graphs indicating the stimulus conditions (x-axis = visual azimuth, y-axis = time).

For imaging responses, flies were shown a perspective-matched version of the stimulus from our behavioral assays. The imaging region contained many local dendritic processes belonging to multiple individual columnar neurons (indicated in Figure 21A). To test for neuronal responses that could underlie the figure-perceptual computations that we know flies make, we first recorded responses to a 30-degree bar sweeping across the azimuth of the LED display. The bar stimulus activated sequential retinotopic columnar elements as the bar swept across the azimuth

(indicated in Figure 21A, monochrome image with pseudocolor mask). Within the image frame, we recorded from multiple regions of interest (ROIs), which are arranged in order along the nasal-temporal axis (Figure 21B *top*). The width of GCaMP excitatory response corresponds with the width of the bar (roughly 30-degrees) passing through the receptive field of the ROI. We did not identify any significant response variation along the n-t axis, indicating that the ensemble of columnar elements responds similarly to the sweeping bar. We therefore collapsed the spatial dimension in order to pool responses across ROIs in time (Figure 21B *bottom*). All classes of lobula projection neurons showed similar retinotopic homogeneity.

We compared the mean  $\Delta F/F$  response to switching the entire LED arena ON and OFF (Figure 21C). The response amplitudes within dendritic arbors to ON and OFF were very small in each cell type, indicating that lobula projections neurons are strongly tuned to motion and other motion-derived features rather than flicker.

We presented a battery of 16 stimuli, only a few of which are highlighted here as a proof-of-concept. LC10a shows no difference in response to the two directions of Ground-alone stimulus, but shows a very different response to a “receding curtain” stimulus (Figure 21D arrow). This is perhaps unexpected because the receding-curtain-type stimuli begins as a wide-field stimulus and only changes when the discontinuity of the edge passes through the visual field leaving behind a *static visual scene*. This demonstrates that LC10a has a strong predilection for the *non-EM* components of the stimulus.

By contrast, LC12 shows nearly identical responses to ground motion in each direction, while the two directions of Fourier bar motion elicit markedly different responses (Figure 21E). By contrast, the Theta bar responses are nearly identical (Figure 21E double arrow). In combination, these suggest a mechanism whereby the contributions of both FM-direction and EM-direction *and* size-tuning interact in a multivariate way. Taken together, these two cell classes demonstrate properties of complex EM and FM coding in a manner similar to that Lee and Nordström found in the lobula plate. These are exciting developments because collectively these results demonstrate the first clear evidence for the underlying neural mechanism of higher-order motion coding in the fly visual pathway.

However, the examples shown demonstrate the difficulty of systematic evaluation of responses within a particular neural sub-type across stimulus-conditions to produce conceptual models for the underlying coding filters that these cells implement. Which stimuli match the underlying neural filter the best? How will we know when we’ve identified the receptive field properties of cell classes that by definition extract abstract representations of visual features? To address this shortcoming in a methodological manner, we have undertaken a graph theoretical covariance analysis that considers all possible pair-wise comparisons between responses to our battery of 16 stimuli that parameterize the figure-ground space. Stimuli are then schematized as nodes, and those that elicit statistically indistinguishable responses within a particular cell-type are connected by an edge, and the ensemble of tested stimuli can then be viewed as a graph. This work is ongoing and is under production for publication – submission is planned for the first week of December, 2014.

## 3.6 Mechanisms and Models

### 3.6.1 Context established by initial work

It is clear from the results obtained from this and the prior AFOSR-sponsored work that flies do not rely (strictly) on outputs from classical EMDs to detect visual figures, as previously

hypothesized [18][46]. Rather, they display computational capabilities previously thought to be the domain of vertebrate nervous systems, in that they are able to respond to differences in higher-order spatiotemporal statistics between figure and background. In their initial study of the electrophysiology of the LPTC H1, in which they first noted an unexpected sensitivity to higher-order motion, Quenzer and Zanker [45] postulated that the canonical EMD might still be able to support such sensitivity in conjunction with additional nonlinearities or more complex architectures (i.e., rectification of the inputs to EMDs, and/or multiple cascaded EMD units). However, although simulations were run and the results presented graphically, quantitative data were not given to support this hypothesis.

The electrophysiological results from HS and VS cells documented in our PNAS paper [32] are fascinating but raise as many questions as they answer. Sensitivity to higher-order figure motion is associated with large variances in the neural responses, and it seems to be distributed piecemeal between the different parts of the receptive fields and on different phases of the input stimuli. This suggests that the quasilinearity observed at the behavioral level may be cobbled together from distinctly nonlinear parts. But overall, the nature of higher-order sensitivity in the HS and VS cells is itself uncertain: are these neurons primarily integrators of EMDs that happen to be modulated by lateral projections from dedicated figure-detecting cells, or are *all* LPTCs simply integrators of varying proportions of first-order and higher-order motion inputs?

The first year's efforts were largely consumed with characterizing the phenomenon of higher-order motion sensitivity, including design and performance of experiments and development and application of analytical techniques to interpret the results. Modeling efforts were confined to the last two years of the grant. During the second year, we developed an explanatory model for the response characteristics of the novel neuron cSIFE, and in addition developed a biophysical model for the correlator function that is thought to underlie first-order motion detection. We also proposed that two sequential stages of computation, presumably implemented in the higher optical ganglia, contribute to figure sensitivity. One is assumed to comprise some fundamental, local set of neurocomputational primitives, possibly including (but not necessarily limited to) the neural analog of the Reichardt correlator, and a second constitutes some means to compute spatial disparities between these in order to distinguish figure from background. During this period, we followed up on this postulate, and examined how sets of correlator circuits, operating on a *range* of local signals, might serve as primitives for the detection of spatiotemporal differences in imagery across a figure boundary. In addition, we modeled a neural implementation of a winner-takes-all function (which is not directly related to neural circuits studied so far during the project, but arose out of Shoemaker's interest in NMDA receptor-based computation, which formed the basis for one of the correlator circuits modeled in Year 2).

### 3.6.2 Modeling of cSIFE

In our Journal of Neuroscience paper we suggested a model input for how cSIFE may derive its high sensitivity to flicker, and strong inhibition by stationary patterns (Figure 22). In the proposed circuit early visual input is separated into ON and OFF luminance changes, which could be done via half-wave rectification in L1 and L2, respectively [4]. In our model circuitry, the ON and OFF output is further separated into an inhibitory (blue) and an excitatory (red) pathway (Figure 22A).

The ON and OFF inputs are processed independently via temporal high-pass filters (HP, Figure 22A), leading to excitatory responses to high-frequency, high-contrast luminance changes (as in Figure 17). Unlike the EMD, there is no spatial correlation between neighboring inputs in



the excitatory pathway (see Figure 22A). This leads to larger responses to full-screen flicker than to drifting gratings with the same temporal frequency (Figure 16), and greater sensitivity Figure 15 to lower spatial frequencies (Figure 17B), since these generate stronger luminance changes at the level of individual photoreceptors. Similarly, the lack of spatial correlation leads to insensitivity to the direction of motion (Figure 15E).

For inhibition by stationary patterns the ON and OFF signals are first processed in temporal low pass filters (LP, Figure 22A). The ON signal from one input is then subtracted from the OFF signal from a spatially separated input ('-', Figure 22A), and vice versa (not shown, for simplicity). The lateral inhibition between inputs of opposite contrasts leads to inhibitory responses to stationary, high-contrast patterns (Figure 15A, C).

The temporal low pass filter (LP, Figure 22A) suggests that extremely slow-moving patterns should also generate inhibition. Indeed, the response to a 0.5 Hz sinusoidal grating is inhibited compared with the spontaneous rate (Figure 17A, N=4). In the publication we performed one direct test of the model circuitry (Figure 22B), but we will eventually expand on this set of experiments using a range of artificial and natural images that we are manipulating in space and time

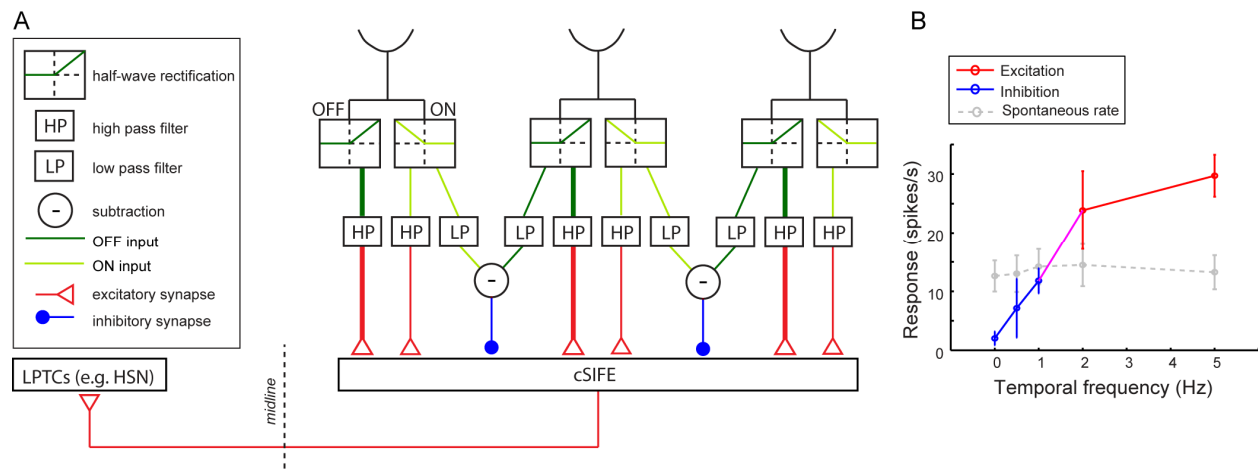


**Figure 22: Proposed input circuitry to cSIFE. A.** The diagram shows a proposed input circuitry to cSIFE. Early visual processing is separated into ON and OFF pathways, here shown as half-wave rectification. The ON and OFF inputs are then either subjected to temporal high-pass filtering (HP), or low-pass filtering (LP), followed by subtraction of the opposite contrast from a neighboring unit (-, only one polarity shown here). The high-pass filtered output leads to excitatory responses in cSIFE (red), whereas the subtracted output leads to inhibition (blue). The cSIFE axon crosses the visual midline where it may interact with other LPTCs, such as HSN. **B.** The response of cSIFE to 0-5 Hz sinusoidal gratings (6° wavelength).

### 3.6.3 Modeling of biophysically-plausible 'delay' and 'correlate' mechanisms

The Hassenstein-Reichardt EMD, based fundamentally on a 'delay-and-correlate' operation, has been a dominant model for visual motion processing for over 50 years. In addition, recent work has suggest that 'delay-and-correlate' operations are almost certainly crucial to the detection of small visual targets [59], and we hypothesize that they may also play a role in figure detection. However, although a number of plausible mechanisms exist for a neural 'delay', the way in which a 'correlate' operation might be implemented in a neural substrate remains unclear.

We have conceived a basic neural ‘correlator’ that depends on the action of chemical synapses, in particular the facts that synaptic receptors modulate *membrane conductance* by the opening or closing of ion channels, and that various classes of channels have differing reversal potentials associated with them. Figure 23 shows a minimal neural model in which a correlation-like operation is achieved: excitatory input to a target neuron *N1* is supplied by input channel CH1 and its effectiveness is modulated by changes in the *incremental membrane resistance* of *N1* that are driven by input channel CH2. The effect on the circuit output of CH1 acting alone is nulled out in neuron *N2*.

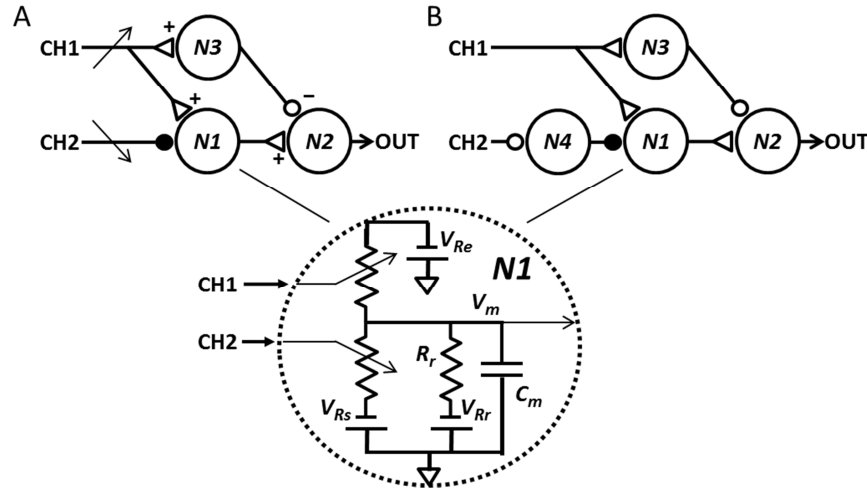


**Figure 23: Proposed Model for a neural ‘correlator’.** Signals carried in two input channels CH1 and CH2 interact. Large open circles represent neurons, open triangles excitatory synapses, small open circles hyperpolarizing inhibitory synapses, and small closed circles synapses that are shunting in their effect. Diagram A depicts the basic scheme. The essential nonlinear interaction takes place in neuron *N1*, for which a single-compartment electrical model is shown at bottom. In this circuit, the node at center represents the cell interior, with instantaneous potential  $V_m$  with respect to the extracellular space (‘ground’). The passive or unstimulated membrane is characterized by resistance  $R_r$ , resting potential  $V_{Rr}$ , and capacitance  $C_m$ . Channel CH1 activates synapses onto *N1* whose ion channels have an excitatory reversal potential  $V_{Re}$ ; channel CH2 *inversely* modulates synapses with an effective reversal potential  $V_{Rs}$  that is equivalent to or very near the resting potential  $V_{Rr}$ . This modulation could, for example, represent shunting inhibition that is *reduced* by activation of CH2, as suggested in Diagram B. In this circuit, *N4* represents an interneuron that imposes tonic shunting inhibition in *N1*, and inhibition of *N4* via CH2 *relieves* this tonic inhibition. The neuron *N2* performs a nulling function: its two inputs are weighted such that, in the absence of activity in channel CH2, the effect of excitatory input from *N1* is nominally canceled by inhibition via interneuron *N3*. As CH2 is activated, the effectiveness of excitation of *N1* by CH1, and consequently of *N2* by *N1*, increases in a graded fashion, and the inhibition in *N2* is overcome.

The suggestion that modulation of membrane resistance in this circuit might be implemented by relief of shunting inhibition is related to the longstanding notion that shunting inhibition could serve as a mechanism for neural gain control and/or arithmetic division. One issue with its application to a *multiplier* is that the modulation of conductance by input CH2 results in a supralinear dependence of the circuit output on that signal. However, this characteristic would be counteracted by a number of biophysical phenomena associated with neural function – including



limits on vesicle release in presynaptic neurons, limits in the number of receptors available postsynaptically, and saturation of membrane potential in the postsynaptic neuron – that tend to be sub-linear or compressive in their effects. Some simulation results for this network with single-compartment neural models under dc conditions are shown in Figure 24.

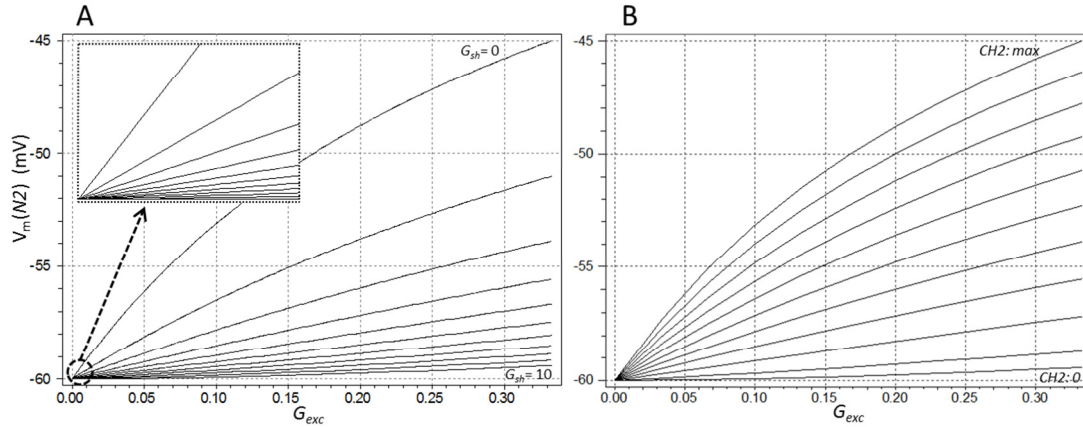


**Figure 24: Parametric multiplier curves for the neural circuits depicted in Figure 23. The ordinate is the membrane potential of N2; the abscissa is excitatory synaptic conductance in N1 commanded by CH1, expressed in terms of passive or unstimulated membrane conductance  $1/R_r$ . Panel A pertains to the 3-neuron circuit of Figure 1A; the parameter is the shunting conductance  $G_{sh}$  in N1 that is decreased by activation of CH2 (also expressed in terms of  $1/R_r$ ). It is varied in increments of 1 unit. The inset shows the small-signal behavior of the circuit with respect to  $G_{exc}$ . Panel B pertains to Figure 1B, and in this model the CH2 input is subject to compressive nonlinearities in neuron N4, which model saturation of available receptors at the input synapses and membrane voltage limiting. The parameter is the strength of the inhibitory input imposed on N4 via CH2, varied in equal increments. The shunting inhibitory conductance in N1 that is driven by N4 is scaled so that it assumes the same total range as in Panel A. The resting, shunting, excitatory, and hyperpolarizing inhibitory reversal potential values are set to  $V_{Rr} = V_{Rs} = -60\text{mV}$ ,  $V_{Re} = 0\text{V}$ , and  $V_{Ri} = -90\text{mV}$ , respectively, and apply to all neurons.**

Of further interest is a second possible biophysical mechanism for modulation of membrane resistance in the interaction neuron N1, one relies on the inherently nonlinear/nonmonotonic electrical properties of the *NMDA receptor* (NMDAR). A negative slope conductance regime associated with NMDARs can result in an *increase* in incremental membrane resistance when they are active in a neuron – and this can give rise to a multiplicative effect in the context of the ‘correlation’ mechanism proposed herein, when the input channel CH2 is associated with NMDA synapses. Such amplifying effects also typically require coactivation of hyperpolarizing inhibitory channels.

DC operating characteristics of such a model are shown below in Figure 25.

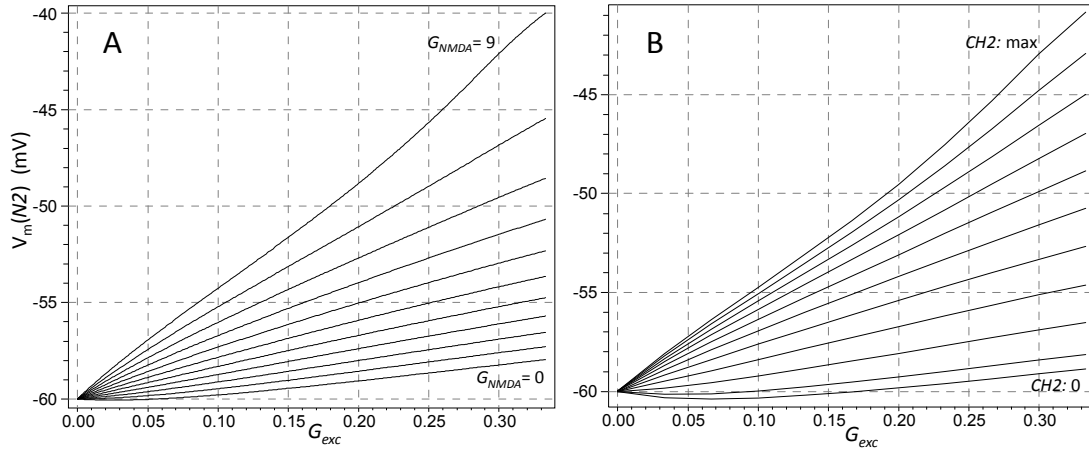


**Figure 25: Parametric multiplier curves for an implementation of the ‘multiplier’ network that relies on the nonmonotonic current-voltage characteristic of NMDARs. The ordinate is the membrane potential of  $N2$  and the abscissa the excitatory synaptic conductance in  $N1$  commanded by  $CH1$ , expressed in terms of passive or unstimulated membrane conductance  $1/R_r$ . Hyperpolarizing inhibitory inputs to  $N1$  are assumed to be activated in proportion to NMDAR activation. In Panel A, the parameter is a measure of the slope conductance  $G_{NMDA}$  of active NMDARs driven via  $CH2$ , varied in equal increments, and also expressed relative to  $1/R_r$ . In panel B, saturation of the number of available NMDARs is also modeled. NMDAR conductance is scaled so that it assumes the same total range as in Panel A.**

One issue with the NMDAR-based model is that co-activation of hyperpolarizing membrane conductance must be made in strict proportion to NMDAR activation, to prevent offsets in the operating curves. It is difficult to conceive of a mechanism involving inhibitory interneurons that can maintain the required degree of linearity. However, a possible *intrinsic* mechanism to achieve this might be the presence of *SK channels* in the membrane of  $N1$ : channels of this type are activated in proportion to the concentration of calcium conducted into the neuron by active NMDARs. SK channels and NMDARs are in fact found in close association in vertebrate cortical neurons, and the existence of just such a feedback mechanism has been demonstrated in that context [40]. The hyperpolarizing current conducted by SK channels necessarily lags NMDAR activation in time, and thus activation of  $CH2$  in the model alone would cause *transient* depolarization in the model – but such transients are consistent with startup transients observed in motion-sensitive and other higher visual neurons in the insect visual pathway. This concept shows promise in ongoing simulations.

Finally, we are examining the possibility that the kinetics of synaptic receptors in the  $CH2$  signal path might comprise a significant component of the delay operator in a ‘delay-and-correlate’ circuit in insect vision. NMDARs have very slow kinetics for an ionotropic receptor, and  $GABA_B$  receptors – which are a likely mechanism for shunting inhibition in the original circuit of Figure 23 – are metabotropic and even slower. Simulation of the temporal frequency response of an elementary motion detector using linearized models for vertebrate receptors of these two types show optima at frequencies *below* (although within an order of magnitude of) similar curves derived from motion-sensitive neurons in insect brains, as suggested in Figure 26. (It should be noted that these optima *are* similar to those seen in crepuscular and nocturnal insects.) Both receptor types are subject to the effects of allosteric neuromodulators, which could provide a mechanism for (real-time) modulation of the tuning or gain of EMDs.

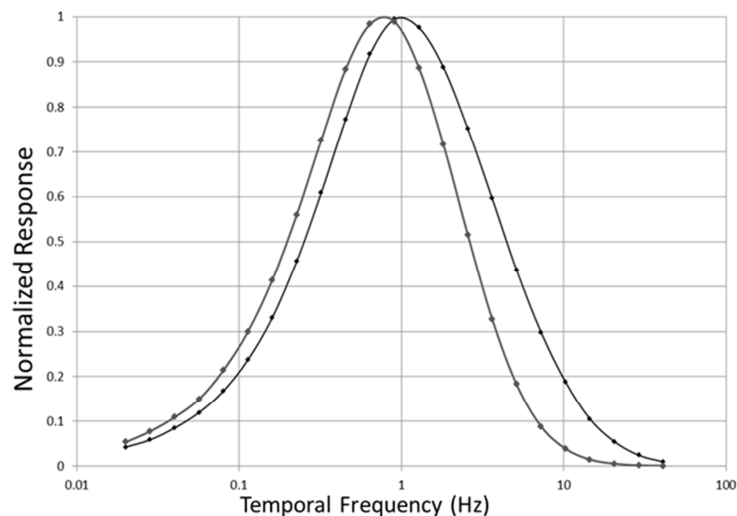


**Figure 26: Temporal frequency tuning of Hassenstein-Reichardt EMD with delay operators based on receptor kinetics. The ordinate is EMD output normalized by its maximum value for each curve. The gray curve is for GABA<sub>B</sub> and black for NMDA receptors. There is no prefiltering or prior nonlinearity used in the model.**

These findings were presented in a poster entitled “A biophysical model for neural ‘delay-and-correlate’” at the ICIV conference in 2013.

#### 3.6.4 Fundamental computations underlying figure detection

As noted in the introduction, during the course of the project we introduced the hypothesis that correlations or product-like operations computed pairwise over a variety of different visual signals might provide a primitive basis for detection of the presence of a figure (or figure boundary). In the final year of the project, we have initiated a study to test this hypothesis.

The inspiration for this approach comes from models for motion detection functions in the insect visual system. The well-known Hassenstein-Reichardt correlator [24] (although its biophysical substrate remains unknown) has been accepted for years as a model for local motion detection, and is believed to constitute the computational primitive that underlies analysis of wide-field motion [25][36][50]. This model involves a pairwise, product-like operation between delayed local and undelayed neighboring visual signals (or *vice-versa*). Recent work suggests that these are derived from separate ON and OFF channels that are segregated earlier in the visual pathway [30]. The Reichardt detector, however, is not the only form of motion detection that has been modeled with a ‘correlator’. Research on *small target motion detecting* neurons (STMDs) provides evidence that a product-like operation also underlies the sensitivity to small dark targets that is observed in these cells [59][60] – although in this case, the ‘correlation’ involves local delayed OFF vs. local undelayed ON signals, each with highly transient response characteristics.

This has led us to postulate that such product-like operations might act as computational primitives for more general forms of spatiotemporal analysis, including the detection of figures or figure boundaries. With this in mind, we began by considering a range of signals known or believed to be present in each visual unit of the lamina and/or medulla, which might comprise the inputs for an expanded set of correlators that could serve this purpose. These include the aforementioned ON and OFF channels, with additional characteristics including transient [29] or

sustained [28] temporal responses, and delayed versus undelayed signal pathways. A schematic diagram illustrating the concept is shown below in Figure 27:

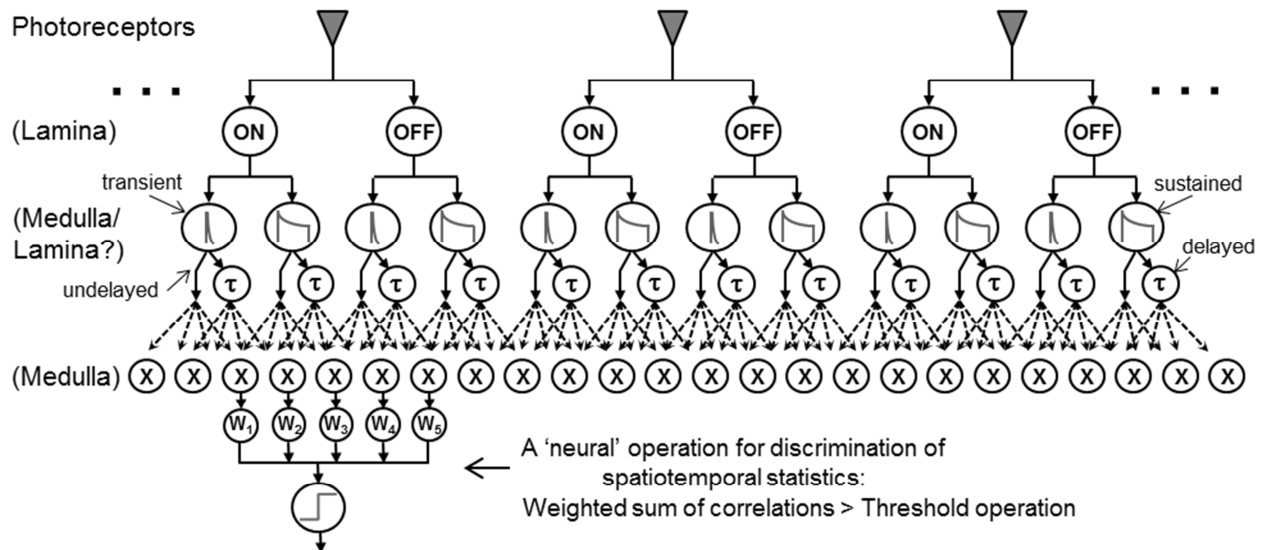


**Figure 27: Schema for spatiotemporal processing that is hypothesized to support figure detection. Signals from photoreceptors are segregated into ON and OFF channels, with the former responding to increments in luminance, and the latter to decrements. These are further segregated into channels with transient or sustained response characteristics (with the sustained channels emphasizing high-frequency components but having a finite dc response). Each of these may be routed by delayed or undelayed pathways to a set of 'correlators', presumed to reside in the medulla and each represented by a circle with an 'X' at its center. At bottom left is shown a hypothetical, 'neuro-plausible' unit for spatiotemporal discrimination, which consists of a weighted sum of correlator outputs cascaded with a thresholding operation.**

We considered signals with every possible combination of these attributes, leading to a set of eight per visual unit. For generality, we also considered every possible product formed between the set of signals that are either internal to a visual processing unit or arise from its nearest-neighbor units. This leads to 28 possible internal products (neglecting the simple square terms that arise from multiplying a signal by itself), and 64 products with signals from each neighbor. These are assumed to form the basis for the discriminations that allow the system to detect different spatiotemporal statistics across a figure boundary.

We propose a simple, 'neuro-plausible' model for a unit that could perform such discriminations in the form of a weighted summation (corresponding to the action of weighted input synapses) of outputs from some subset of correlator units, followed by a thresholding operation. With a 'hard' threshold and binary output, such a unit could be interpreted as estimating a strict class membership function: it is intended to be active when the spatiotemporal characteristics of its inputs fall within a certain range, and inactive otherwise. One such unit is depicted at bottom left in Figure 27. It is assumed that such units would be repeated retinotopically, each having a consistent, spatially-shifted receptive field (corresponding to the projections from its corresponding set of correlators). It is also supposed that multiple classes of

such units might exist, each ‘tuned’ to discriminate according to some particular criterion that would be determined by its individual weighting pattern.

In preliminary work on these concepts, we developed a numerical model for the network architecture suggested in Figure 27. The photoreceptor is represented with an adaptive Naka-Rushton equation [37] (adaptation time constant  $\tau = 1\text{s}$ ), and ON/OFF segregation by a first-order highpass filter ( $\tau = 200\text{ms}$ ) followed by half-wave rectification for each phase (with the OFF phase inverted so that both channels carry positive signals). The ‘sustained’ temporal characteristic is modeled with a ‘relaxed’ linear highpass filter ( $\tau = 50\text{ms}$ ) that passes 40% dc. The ‘transient’ characteristic is based on the nonlinear transient cell model of Wiederman, Shoemaker, and O’Carroll [60]. The delay operator is a first-order lowpass filter ( $\tau = 50\text{ms}$ ). The ‘correlators’ are modeled as simple products.

The discrimination function is modeled as two-state vector quantization on the set of correlator signals that form the ‘receptive field’ of the discriminator unit. An input vector is associated with one class or the other according to which of two *prototypes* it is closest to by Euclidean distance. It is straightforward to show that this geometrically-defined procedure yields the same result as a weighted summation and thresholding, where the weighted sum is the inner product of the input vector and the (normalized) difference vector between the two prototypes, and the threshold is equal to the projection of the midpoint between the prototypes onto an axis parallel to the difference vector and passing through the origin. (Naturally this holds for any weight set and threshold proportional to these values.) This formulation allows us to use clustering algorithms to determine an optimal or near-optimal weight set over some ensemble of inputs that can be divided *a priori* into two classes (e.g., a class that originates within a figure and a second that originates without). Presumably, if a similar scheme for discrimination were present in the fly, then evolutionary pressures would likewise have driven the synaptic weights toward optimal values. To optimize the prototype vectors / weights, a multi-start iterative procedure was used. This implemented the *k-means* clustering algorithm (with  $k=2$ ) when it resulted in improvement in classification at a particular iteration, and a heuristic method of prototype adjustment when it did not. (As is typical with nonlinear optimization, there is no guarantee of finding a global maximum with this method, but multiple trials suggest that it can come close.)

An initial set of simulations has been run to test this model with a small network containing a one-dimensional array of eight ‘photoreceptors’ and their accompanying visual processing units. Correlations were formed between the internal signals, and with the neighboring signals, for the central six units in this array. Sequences of time-varying imagery were generated to form the input data for these simulations. To date, these have been derived from photographic data of natural imagery, so that spatial statistics are similar to those that might be encountered by an animal in its environment. In each series of input data, there is a sharp boundary at the center of the image with different spatiotemporal characteristics in each half – for example, motion on the left and flicker on the right – and no correlation across the boundary (i.e., the halves are derived from different parts of a panoramic master image). To form the inputs to the model network, the image sequences are downsampled onto a  $1 \times 8$  grid with a spatial separation of  $1.25^\circ$ , and blurred by spatial convolution with a Gaussian kernel that has a half-maximum width of 1.4 times this value, in order to mimic the antialiasing properties of compound eye optics. These parameters yield ‘retinal’ images with resolution similar to that in larger fly species (such as *Eristalis*). The (blurred) boundary at the center of the image defines a stationary ‘figure edge’ that is located between the left and right sides of the model array. As suggested by work in the

Frye lab reported herein, such edges or boundaries appear to be the key features that are exploited for figure detection in the fly.

Initially, five classes of figure boundaries were generated, with the following attributes on the two sides of the array:

- Static pattern vs. coherent motion
- Static pattern vs. flicker
- Motion vs. flicker
- Motion left vs. motion right
- Flicker vs. high-frequency flicker

It soon became apparent that the scenarios with static patterns were trivial cases as far discrimination, due to the lack of temporal variation in the downstream visual signals. Simulations focused on the final three scenarios, and data were generated from five different natural images for each, with 35,000 total samples generated at 10ms sample intervals. Output data were sampled at the same rate. Moving imagery was animated at 50°/s, and flicker at the lowest frequency was obtained by animation perpendicular to the array axis at the same speed. Flicker at five times this frequency was obtained by dithering randomly between different regions of the master image at an appropriate rate, with smoothing between image changes.

Vector quantization into one of two classes was performed and optimized based on the outputs of the correlators in the array, independently for each scenario. This is equivalent to assuming the existence of a distinct class of optimized ‘neural discriminator’ for each. Furthermore, the correlator outputs were arranged in different groupings corresponding to different possible ‘receptive fields’ for the discriminators. One grouping included all correlations with at least one factor arising from a particular visual processing unit (i.e., 28 internal signals and 64 in association with each neighbor, for a total of 156), and another only the correlations between neighbors (64 signals). Note that discriminators with the first grouping have overlapping receptive fields.

Discrimination capability was evaluated and scored according to what fraction of the outputs from each of the two classes was grouped together, evaluated over both classes and all samples for a given input scenario. (Note that purely random class assignment in this two-class problem would result in a score of 50%.) For the unit-wise receptive fields, the two classes corresponds simply to the location of a unit in the left or the right half of the image. However, for the smaller inter-unit receptive fields, in addition to left-right partitioning, the correlations *across* the figure boundary were compared to correlations originating entirely from *within* either the left or right side. Figure 28 below illustrates discrimination performance:

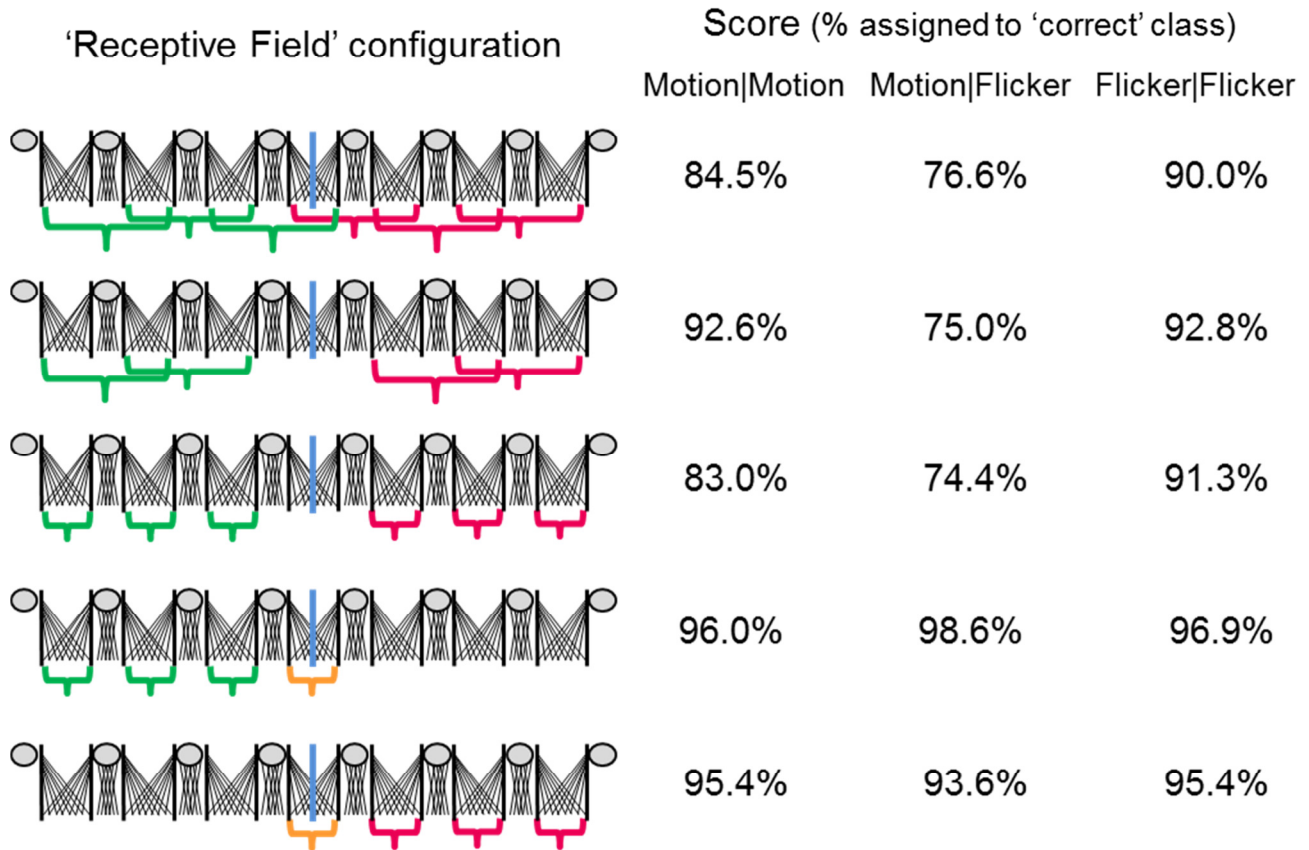


**Figure 28: Scoring of discrimination of differing spatiotemporal statistics according to the scheme described in the text. Inputs with differing spatiotemporal statistics are presented to the right and left halves of the visual processing array, as indicated by the headers in the three columns of data at right. In the ideograms at left, visual processing units are indicated by gray circles, internal correlations by the intersecting lines under each circle, and inter-unit correlations by intersecting lines between them. Location-based partitioning of discriminators into two classes is indicated by different colored brackets that extend over the receptive fields of each class. Scores in each row indicate the percentage of the time (i.e., the fraction of samples) that the discriminator outputs for one class are the same and in the opposite state from those of the other class, for each of three input scenarios. The top two rows show results for unit-wise receptive fields, and the bottom three rows, for inter-unit receptive fields. In the scoring for the bottom two rows, each discriminator on the side (receptive fields in green or red) is compared individually to the central discriminator, and the score compiled over all three comparisons. Significance of the results is discussed in the text.**

In the results shown in Figure 28, note that an independent optimization has been performed for each input scenario indicated in the columns at right, and for the receptive field configurations shown in each row. For the unit-wise receptive fields (top two rows), when the central discriminators (which both receive inputs from the cross-boundary correlators) are excluded, the result is a modest improvement in performance for two of the three input scenarios. When inter-unit receptive fields that arise exclusively from units on one side or the other (third



row) are considered, scores are similar to those for the unit-wise receptive fields. However, when the receptive field that extends across the figure boundary (coded in orange in rows 4 and 5) is compared to those arising from one side or the other, the discrimination scores are consistently higher than for the other cases, being above 90% in all cases.

A single important lesson can be drawn from these results: in a correlation-based scheme for spatiotemporal discrimination to support figure detection, it is the *correlations across figure boundaries that appear to carry the most information with respect to discrimination*.

The vector quantizations described above are based on a very high-dimensional vector space, i.e., that of every possible product of signal pairs of the various assumed types. Although each medullar column contains an impressive amount of neural machinery (>350 individual cells or processes thereof, from ~59 cell types [54]), it is perhaps unrealistic to expect that on the order of 60-150 correlations can be implemented per medullar column. It is therefore pertinent to ask how well discriminations can be made based on smaller subsets of these correlations. We have performed a few additional simulations and optimizations in which only the ‘most informative’ correlations were retained. These were judged to be the components of the two prototype vectors (as obtained from the original simulations) with the largest relative differences in their magnitudes. Figure 29 shows the results of these experiments:

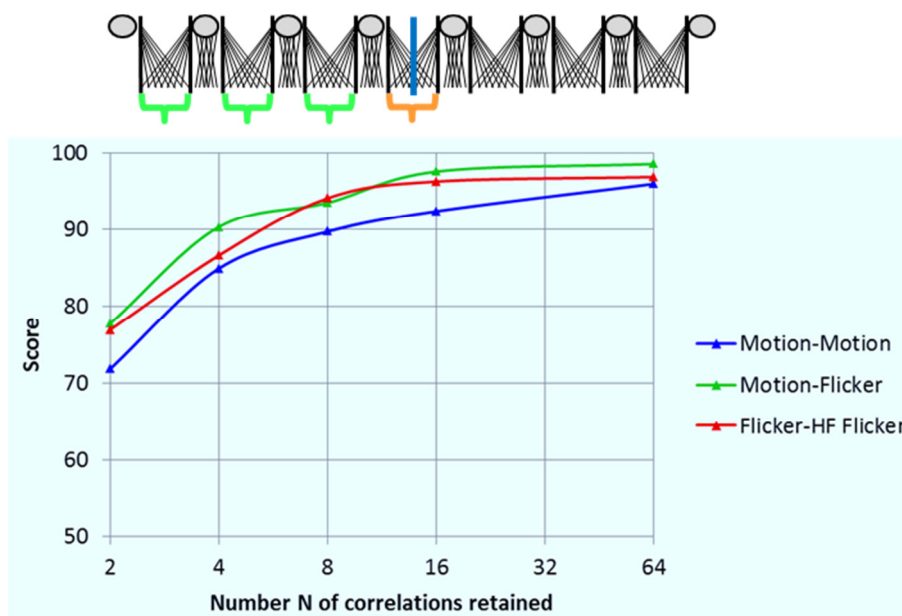


**Figure 29: Scoring of discrimination as a function of the number of correlations retained in the receptive field, for the case in which the central inter-unit discriminator is compared with each of the left-side discriminators. (Note the abscissa is on a log scale.) An independent optimization was performed for each datum.**

From these results, we conclude that even on the order of ten of the most informative correlations carry substantial information for discrimination of differing spatiotemporal statistics.

What is the nature of the particular products that by our criterion are the most informative? The majority of them involve at least one transient signal, and interestingly, *all* of them involve at least one delayed signal. In addition, there is substantial overlap between the sets of products

that are most informative for each of the three different input scenarios used in the simulations. This, like the results in Figure 29, suggests that effective and *general* discrimination under this scheme could be accomplished with a biologically plausible number of correlation operations.

Further work on these concepts, including consideration of moving boundaries, and of other input scenarios (including, for example, those used in our experiments), will be undertaken in the project extension if granted.

### 3.6.5 Winner-takes-all neural circuit with NMDA receptors

In simulation and analysis, we demonstrated that a neuronal network with lateral feedback inhibition, arranged in perhaps the simplest possible topology, is capable of realizing the winner-takes-all (WTA) function. WTA is a powerful computational primitive that is often attributed to biological nervous systems. The neural circuit is illustrated in Figure 30.

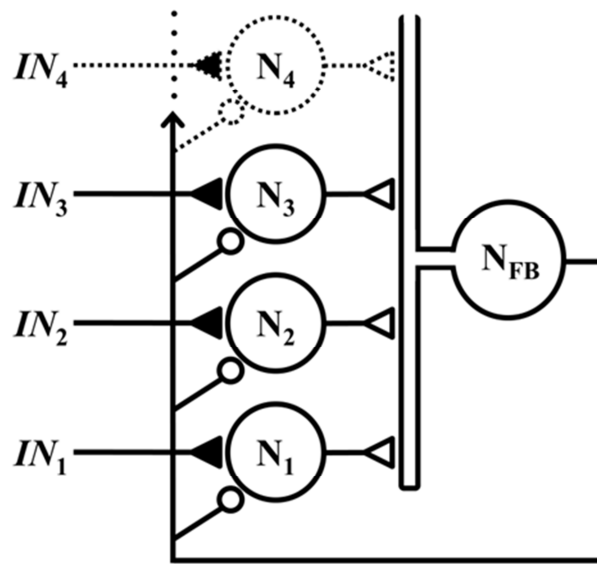


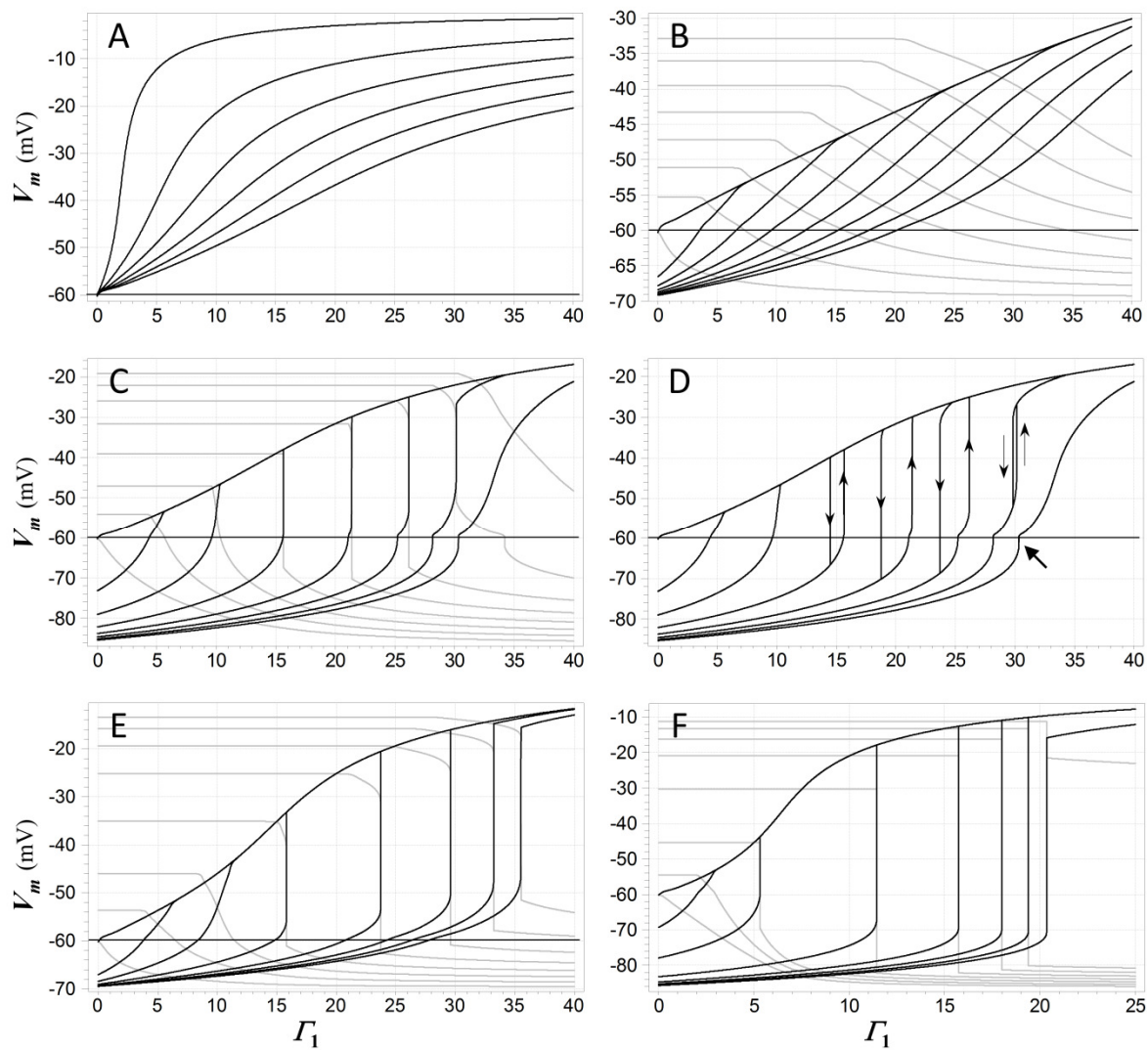
**Figure 30:** Members of a set of competitive neurons  $N_1, N_2, N_3, \dots$  each receives a respective excitatory input  $IN_1, IN_2, IN_3, \dots$ , via an NMDA synapse (closed triangle). These neurons form excitatory synapses (open triangles) onto a common interneuron  $N_{FB}$ , which projects feedback to all neurons in the set via inhibitory synapses (small open circles). Although not depicted, the outputs of neurons  $N_1, N_2, N_3, \dots$  are assumed to also project to other parts of the nervous system.

Excitatory inputs to the network are assumed to be supplied by synapses incorporating *NMDA receptors* (NMDARs), a class of glutamatergic receptor that is found in many phyla and frequently associated with synapses. Although nonlinearities such as neural thresholding contribute to the winner-takes-all regimes that can be achieved by this network, these depend most critically on the unique electrical properties of the NMDAR ion channels, which have a nonmonotonic current-voltage relationship under physiological conditions [27], with a negative slope conductance region that is due to (kinetically fast) magnesium blockade. This characteristic renders the NMDAR capable of supporting neural amplification and bistability in conjunction with other membrane conductances [49]. The primary finding of this novel work is that a WTA characteristic can be *induced* by high-gain regimes that result from such interactions, rather than

requiring a high intrinsic or parametric gain in the feedback loops. This is significant because it represents a mechanism for WTA that is both simple and at the same time biophysically plausible, relying on known characteristics of ubiquitous classes of synaptic receptors.

A simple model of this network was developed for numerical analysis, and used for the simulations reported herein. The high-gain behavior that is associated the WTA function with is enhanced when the total non-NMDAR conductance has a reversal potential below typical neural resting potentials, and also when its current-voltage dependence is sub-linear or inward-rectifying [47][49]. With this in mind, behavior of the network was examined in simulations for inhibitory feedback with several different characteristics: either mildly hyperpolarizing (e.g., as might be expected if chloride channels were associated with the inhibitory synapses) or more strongly hyperpolarizing (which might be expected with potassium channels), and having either ohmic or inward-rectifying channels. Gamma-aminobutyric acid (GABA)-mediated synapses, which are prime candidates to implement the lateral inhibition, occur in two major classes that reflect different combinations of these characteristics – the GABA<sub>B</sub> class involves Kir channels, which conduct potassium and are inward-rectifying (and thus might be expected to promote high-gain behavior), whereas GABA<sub>A</sub> receptor channels conduct chloride and are non-rectifying.

Figure 31 below illustrates some of the dc transfer characteristics seen in this network for various configurations:



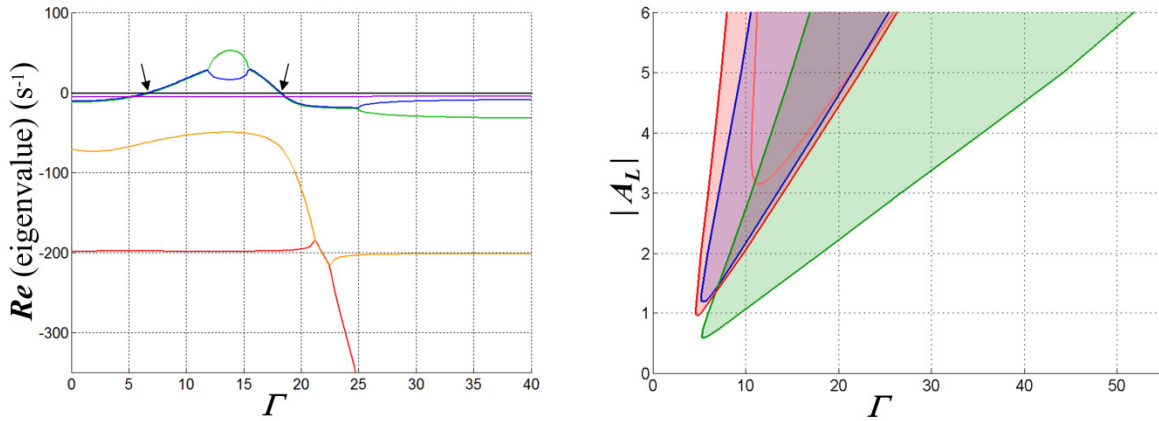
**Figure 31 (previous page):** *A*: a dc input-output characteristic for the network when only a single competitive neuron  $N_1$  is activated. The inhibitory feedback synapses are ohmic/strongly-hyperpolarizing. The abscissa is the normalized conductance  $I_1$  of the input (NMDA) synapse onto the neuron, the ordinate is its membrane potential, and the parameter is the loop gain constant  $A_L$ , which is varied from 0 to  $-5$  in decrements of  $-1$ . *B–F*: dc transition characteristics for several configurations of the network when two neurons receive excitatory input. The loop gain constant  $A_L = -4$  in each case. Input  $I_1$  is swept in individual trials, and the parameter is the input  $I_2$  to the second neuron  $N_2$ , which is fixed during each sweep of  $I_1$  but varied from trial to trial. Membrane potential  $V_{m1}$  of  $N_1$  is shown in black and  $V_{m2}$  of  $N_2$  in gray. In *B–D*, the inhibitory channels are ohmic and  $I_2$  is stepped from 0 to 35 in increments of 5. In *B* the inhibitory reversal potential is  $-70\text{mV}$ ; in *C* and *D* it is  $-90\text{mV}$ . *C* shows results for upward sweeps of,  $I_1$  while *D* shows  $V_{m1}$  for sweeps in both directions, which trigger transitions at juxtaposed limit points and illustrate the presence of hysteresis. Directions of transitions are indicated by thin arrows. The heavy arrow at lower right points to a small secondary hysteresis loop (not fully visible at this resolution). In *E* and *F* the inhibitory channels are inward-rectifying, and  $I_1$  is swept upward in both cases. In *E* the reversal potential is  $-70\text{mV}$  and  $I_2$  is stepped from 0 to 35 in increments of 5; in *F* the reversal potential is  $-90\text{mV}$  and  $I_2$  is stepped from 0 to 17.5 in increments of 2.5. Resting potential in all cases is  $-60\text{mV}$ .

Figure 31A shows the dc input (expressed as NMDAR conductance  $I_1$  relative to the resting membrane conductance) versus output (membrane potential) relationship for a single competitive neuron  $N_1$  when that neuron is the only one in the network receiving excitatory input. The loop gain constant is the parameter. Membrane potential varies smoothly with input activation, and as might be expected, the slope of this relationship decreases as the strength of inhibitory feedback is increased. Figure 31B–F show the behavior of different configurations of the model when two of the competitive neurons receive excitatory input, and the network transitions from one ‘winner’ to another as the first input exceeds the other. (It should be noted that this transitional behavior applies not just to the two-input case, but to *any* situation in which the two neurons with the largest inputs are the only ones that are able to reach a state of depolarization). When the inhibition is ohmic and mildly hyperpolarizing (Figure 31B), the transitions are gentle and the network cannot reasonably be characterized as winner-takes-all. In the remaining cases, however, there are input ranges for which the transitions are not only sharp but discontinuous. These discontinuities and the hysteretic effects that accompany them are associated with bistable regimes. Such a regime prevails over the range of  $I_1$  values bounded by each hysteresis loop in Figure 31D. In these regions, fixed-point solutions exist in which *either* neuron may be significantly depolarized (i.e., in a ‘high’ state), while the other is either hyperpolarized or depolarized to a lesser extent (in a ‘low’ state). Which of the two solutions might be assumed under quasistatic conditions depends on the history of excitation of the system. The discontinuous jumps depicted in Figure 31C–F represent *limit point* transitions, which occur at *fold bifurcations* that correspond to the boundaries of bistable regimes. Outside of transitions between winners, the state of the winning neuron depends on its input level, and thus carries analog information about that input.

The fixed-point solutions in this network model, including its bistable/WTa regimes, are shaped by a rich array of nonlinearities, including the NMDAR current-voltage relationship and the neural thresholding function, but also the rectifying characteristics of Kir channels (if present) and saturation of the membrane potential in a ‘winning’ neuron. Numerical analysis was used to characterize these in more detail, and shows their structure can be quite complex. Some important results may be summarized:

- When bistable WTA behavior is possible, its appearance requires some minimum value of the loop gain;
- When more than two neurons receive excitatory input, then *multi*-stable winner-takes-all states are possible;
- WTA regimes ultimately collapse and *vanish* when the inputs become sufficiently large. This is due to the fact that at high input levels, saturation of the membrane potential in the winning neuron begins to limit the recruitment of inhibition;
- When WTA behavior is supported, behavior is qualitatively similar for inward-rectifying and non-rectifying inhibition, but bi-/multi-stable behavior is more pronounced: it is supported at higher inhibitory reversal potentials and at lower values of the loop gain parameter than when the inhibition is ohmic, and hysteresis is more extensive as well.

In addition to the dc characteristic of the model, its time-domain and ac behavior were also examined. An important question is whether the fixed points identified by the stationary analysis are stable or unstable in nature; the answer is determined by the dynamical characteristics of the inhibitory feedback in conjunction with the input state and other network parameters. Analysis shows that the network may be prone to destabilization when there are two or more independent states in the feedback loop that contribute to lags in its response – and this is certainly the case in a biologically-realistic scenario which accounts for the membrane capacitance of the inhibitory interneuron in the feedback loop, as well as the kinetics of synapses in the feedback path. When these lags and the loop gain are sufficiently large, destabilization occurs as the network inputs approach a magnitude that supports a WTA regime – but interestingly, the network tends to *re-stabilize* at some point as inputs increase further. This is illustrated in Figure 32:



**Figure 32:** Graphs illustrating the fixed-point stability characteristics of one configuration of the WTA network when a single input is active. Inhibitory synaptic conductance is inward-rectifying with reversal potential  $-70\text{mV}$ . The resting membrane time constant  $\tau_R$  in the competitive neuron is set to  $20\text{ms}$ ; membrane charging in the inhibitory interneuron is modeled with a pole with time constant  $5\text{ms}$ , and is cascaded with a four-state model for  $\text{GABA}_B$  receptor dynamics [6] that introduces three additional poles in the feedback path. At left are depicted the real parts of the poles of the closed-loop system at its fixed points as functions of the input strength  $\Gamma$ , in this case for  $A_L = -4$ . Each is coded by a different color. Where two curves overlies, the corresponding poles are complex conjugates. The arrows indicate the points at which a complex pole-pair transitions between left- and right-half-planes and bracket an input range over which the fixed points are unstable. In the middle part of this region, the poles are real and distinct, implying exponential divergence of trajectories away from the fixed point – but large-signal limit cycles (i.e., oscillations) are ultimately assumed by such trajectories. At right, the region over which the network is unstable in the space spanned by  $\Gamma$  and  $A_L$  is shown in red (for purposes of comparison, the pink curve shows the boundary of this region when  $\text{GABA}_A$  kinetics are substituted for  $\text{GABA}_B$ ). In the blue area the membrane conductance in the competitive neuron is negative for the input and inhibitory states at the fixed point, and in the green, WTA bistability would be possible if the input to a second neuron were active (and feedback instantaneous).

The results in Figure 32, which apply when a single neuron is active, define a *minimal input range* over which the network is unstable. Further analysis shows that when multiple neurons are activated, instability and the resulting entrained oscillations may occur over even larger input ranges. Stability is lost and regained in all cases via *Hopf bifurcations*.

This scenario of destabilization is generally incompatible with WTA functionality (at least as conceived in this study) when it applies. It is most pronounced (i.e., occurs at lower loop gains and covers a larger range of input strengths) when the slow dynamics of  $\text{GABA}_B$  receptors (as opposed to faster  $\text{GABA}_A$ ) are associated with the inhibitory synapses in the feedback loops. Very small or negative membrane conductance values in the competitive neurons, which are more prevalent when the inhibitory current is modeled as inward-rectifying, also promote instability. Thus, it might be expected that lateral inhibition implemented with  $\text{GABA}_B$  synapses would compromise the ability of such a network to reliably implement the WTA function. However, an important additional finding is that other biologically-plausible characteristics can mitigate against unstable behavior. When a simplifying assumption of linearity in the inhibitory interneuron (used in most simulations) is relaxed and saturating effects introduced, it can squelch



large-signal oscillations and establish a reliable WTA regime (although the network may pass through an unconditionally unstable regime at lower input values to reach it). In addition, the presence of GABA<sub>A</sub> as well as GABA<sub>B</sub> receptors in the inhibitory feedback pathway – a possibility supported by evidence from the biological literature [1] – can have a significant stabilizing effect.

This is a brief summary of results reported in greater detail in a paper appearing in the journal *Frontiers in Computational Neuroscience*.

## 4 Personnel Supported

In Karin Nordström's lab, AFOSR funds supported Ph.D. students Yu-Jen (Frank) Lee and Olga Dyakova. Lee defended his thesis in May 2014, with Prof. Holger Krapp as the Faculty opponent. Lee and Nordström performed most of electrophysiology presented in this report, complemented by behavioral and analytical work performed by Dyakova, who enrolled as a Ph.D. student in September 2013.

In Mark Frye's lab, AFOSR funds supported Ph.D. students Jacob Aptekar and Mehmet Keles, and M.S. student Ross Kelley. Aptekar, who graduated in June 2014, performed flight behavioral analyses, neurogenetics, and two-photon imaging. Kelley, who, graduated in June 2013, performed flight behavioral analyses and neurogenetics. The funds currently support Keles, who is performing flight behavioral analyses, two-photon imaging, and neurogenetics.

At Tanner Research, AFOSR funds partially supported Patrick Shoemaker, senior scientist, who has worked on analytical techniques, theory, and modeling, as well as on supporting experimental design.

## 5 Publications

Seventeen papers for publication in the peer-reviewed literature have appeared, or are under production, with the full or partial support of this grant.

### 5.1 Peer-Reviewed Publications Fully or Partially Supported by this Grant:

Aptekar JW, Keles MF, Mongeau J-M, Lu PM, **Frye MA**, **Shoemaker PA** (2014) Method and software for using m-sequences to characterize parallel components of higher-order visual tracking behavior in *Drosophila*. *Front Neurosci* vol. 8, DOI: 10.3389/fncir.2014.00130.

Aptekar JW, **Frye MA** (2013) Higher-order figure discrimination in fly and human vision, *Curr Biol* 23(16):R694-700.

Aptekar JW, **Shoemaker PA**, **Frye MA** (2012) Figure tracking by flies is supported by parallel visual streams. *Curr Biol* 22:482-487.

De Haan R, Lee Y-J, **Nordström K** (2013) Novel flicker-sensitive visual circuit neurons inhibited by stationary patterns, *J Neurosci*, 33 (21): 8980-8989.

Duistermars BJ, Care RA, **Frye MA** (2012) Binocular interactions underlying the classic optomotor responses of flying flies. *Front Behav Neurosci* 6(6), DOI: 10.3389/fnbeh

Fox JL, Aptekar JW, Zolotova NM, **Shoemaker PA**, **Frye MA** (2014) Figure-ground discrimination behavior in *Drosophila*. I. Spatial organization of wing-steering responses. *J Exp Biol* 217: 558-569.

Fox JL, **Frye MA** (2014) Figure-ground discrimination behavior in *Drosophila*. II. Visual influences on head movement. *J Exp Biol* 217: 570-579

**Frye MA** (2013) Visual attention: A cell that focuses on one object at a time. *Curr Biol* 23: R61-63

Lee Y-J and **Nordström K** (2012) Higher order motion sensitivity in fly visual circuits. *PNAS*, 109 (22): 8758-8763.

**Shoemaker PA** (2015) Neuronal networks with NMDARs and lateral inhibition implement winner-takes-all. *Front Comput Neurosci* 9(12), DOI: 10.3389/fncom.2015.00012

Wasserman S, Lu P, Aptekar JW, **Frye MA** (2012) Flies dynamically anti-track, rather than ballistically escape, aversive odor during flight. *J Exp Biol* 215:2833-2840.

Wasserman SM, Aptekar JW, Lu P, Nguyen J, Wang AL, Keles MF, Grygoruk A, Krantz DE, Larsen C, and **Frye MA** (2015) Olfactory neuromodulation of motion vision circuitry in *Drosophila*. *Curr Biol* vol. 24, pp. 467-472.

### **Papers Submitted or in Production, Fully or Partially Supported by this Grant:**

Aptekar JW, Zolotova NM, **Frye MA** (*in production*) The switch from object tracking to aversion is driven by higher-order feature detection in *Drosophila*.

Aptekar JW, Keles MF, Lu PM, Zolotova NM, **Frye MA** (*in production*) Optic glomeruli encode higher-order visual features in *Drosophila*. To be submitted, *Nature Neuroscience*.

Dyakova O, Lee Y-J, **Nordström K** Natural scene statistics directly affect the response properties of higher-order visual circuit neurons. *In resubmission, Nature communications*.

Lee Y-J, **Nordström K** (*in production*) Figure motion suppresses the response to wide-field optic flow in hoverfly tangential cells.

Lee Y-J, Jönsson O and **Nordström K** (2015) Spatio-temporal dynamics of impulse responses to figure motion in optic flow neurons, Resubmitted to *PLoS ONE*.

### **5.2 Papers by the Principals in Related Areas:**

Fox JL, **Frye MA** (2013) Animal behavior: Fly flight moves forward. *Curr Biol* vol. 23(7): R278-279

Hidayat E, Medvedev A and **Nordström K** (2013) “On identification of elementary motion detectors”. *Proceedings of the International Symposium on Computational Models for Life Sciences (CMLS’2013)*.

Hidayat E, Medvedev A and **Nordström K** (2013) Laguerre domain identification of the elementary motion detector model in insect vision. *Proceedings of the 11<sup>th</sup> IFAC International Workshop on Adaptation and Learning in Control and Signal Processing (ALCOSP’2013)*. 11 (1): 623-628. DOI 10.3182/20130703-3-FR-4038.00070.

**Nordström K** and Gonzalez-Bellido PT (2013) “Invertebrate vision: Peripheral adaptation to repeated object motion”. *Curr Biol* vol. 23 (15): R655-R656. DOI 10.1016/j.cub.2013.06.009.

**Nordström K** (2013) “Robust prey detection in a small nervous system”. *PNAS* vol. 110 (2): 389-390. DOI [www.pnas.org/cgi/doi/10.1073/pnas.1219973110](http://www.pnas.org/cgi/doi/10.1073/pnas.1219973110).

Dunbier JR, Wiederman SD, **Shoemaker PA**, O’Carroll DC (2012) Facilitation of dragonfly target detectors by slow moving features on continuous paths. *Frontiers in Neural Circuits*, vol. 6, doi: 10.3389/fncir.2012.00079.

O’Carroll DC, Barnett PD, and **Nordström K** (2012) “Temporal and spatial adaptation of transient responses to local features”. *Front Neural Circuits*, 6: 74. DOI 10.3389/fncir.2012.00074. IF: 5.3.

- Shoemaker PA** (2014) Implementation of visual motion detection in analog ‘neuromorphic’ circuitry – a case study of the issue of circuit precision. Invited paper, *Proceedings of the IEEE*, vol. 102, pp. 1557-1570.
- Shoemaker PA**, Wiederman SD, and O’Carroll, DC (2013) Can a Competitive Neural Network Explain Selective Attention in Insect Target Tracking Neurons? *Proceedings, 6th International IEEE EMBS Conference on Neural Engineering*, (San Diego, Nov. 2013)
- Wasserman S, Lu P, Aptekar JW, **Frye MA** (2012) Flies dynamically anti-track, rather than ballistically escape, aversive odor during flight. *J Exp Biol* vol. 215:2833-2840
- Wiederman SD, **Shoemaker PA**, and O’Carroll DC (2013) Correlation between OFF and ON channels underlies dark target selectivity in an insect visual system. *Journal of Neuroscience* vol. 33: 13225-13232.

## 6 Interactions / Transitions

### 6.1 Participation/presentation at meetings, conferences, and seminars

#### 6.1.1 Service on Organizing Committees for Meetings:

**Nordström** organized a symposium entitled “Activity generated modulation of motion vision responses” at the 10<sup>th</sup> International Congress of Neuroethology in College Park, MD, August 2012.

**Nordström** co-organized the Insect Vision: Cells, Computation, and Behavior meeting, at HHMI Janelia Farm Research Campus, March 2013.

**Nordström** was a scientific advisor for the International Conference on Invertebrate Vision in Bäckaskog, Sweden, August 2013.

**Nordström** is presently co-organizing the next Insect Vision: Cells, Computation, and Behavior meeting, scheduled to take place at HHMI Janelia Farm Research Campus, April 2015.

#### 6.1.2 Conference Presentations / Posters:

A poster by Fox and **Frye** entitled *Figure-ground discrimination in flying Drosophila* was presented at the Neurobiology of Drosophila meeting, Cold Spring Harbor Labs, October 2011.

**Nordström** gave an invited research seminar called *Salient feature tracking* at the Max Planck Institute for Chemical Ecology, Jena, Germany, 2012.

**Shoemaker**, **Nordström**, and Fox attended the 10<sup>th</sup> International Congress of Neuroethology in College Park, MD in August 2012. Fox gave a talk entitled *Two distinct visual microcircuits required for figure-ground discrimination in flies*. **Nordström** presented a poster entitled *Bar cells: Underlying neurophysiological mechanisms*.

A poster by Aptekar and **Frye** entitled *The horizontal system cells of the lobula plate in Drosophila have dendritic sub-regions that respond to figure motion in both the preferred and anti-preferred directions against a moving ground* was presented at the Society for Neuroscience meeting, New Orleans, LA, November 2012.

A poster by Kelley, Fox, Aptekar, and **Frye** entitled *Two distinct visual microcircuits required for figure-ground discrimination in flies* was presented at the Society for Neuroscience meeting, New Orleans, LA, November 2012.

A poster by Aptekar, Fox, and **Frye** entitled *The horizontal system of cells in the lobula plate of Drosophila have dendritic subregions that respond to figure motion in both preferred and anti-preferred*

*directions against a moving ground* was presented at the Society for Neuroscience annual meeting, New Orleans, LA, November 2012.

**Nordström, Frye** and Fox presented ongoing work at the Insect Vision: Cells, Computation, and Behavior meeting, HHMI Janelia Farm Research Campus, March 2013. **Nordström's** talk was entitled *Feature detection by hoverfly LPTCs*.

**Nordström** gave a talk entitled *Neural mechanisms underlying target tracking* at the Dynamics of Prey Capture and Escape Meeting, at HHMI Janelia Farm Research Campus, March 2013.

**Frye** gave a plenary talk entitled *Olfactory feature detection in flies* at the Tata Institute of Fundamental Research, Genes, Circuits and Behavior, Mumbai, India, March 2013.

**Frye** gave an invited research seminar entitled *Algorithms and neurons for figure-ground discrimination in Drosophila* MRC Centre for Developmental Biology, King's College London, UK, April 2013.

**Nordström** gave a presentation *Figure-ground discrimination in hoverfly tangential neurons* as an invited lead speaker at the Rank Prize Funds: Symposium on the Computational Basis of Early Vision. The Wordsworth Hotel, Grasmere, Cumbria, UK, May 2013.

**Frye** gave an invited seminar *Olfactory feature detection in flies* at the Department of Biology, University of Indiana, Bloomington, May 2013

**Frye** gave the presentation *Multi-sensory feature detection* at the Center for Neural and Emergent Systems, HRL Laboratories LLC, Malibu, CA, May 2013.

**Frye** gave the presentation *Higher-order visual feature detection* at the Cell Press Symposium: Genes, Circuits and Behavior, Toronto CN, June 2013.

**Frye** gave a plenary lecture *Visual course control and feature detection during flight in Drosophila* and **Shoemaker** presented a poster entitled *A biophysical model for neural 'delay-and-correlate'* at the International Conference on Invertebrate Vision in Bäckaskog, Sweden, August 2013. Both PIs interacted with AFOSR Emeritus Willard Larkin.

**Nordström** gave the presentation *Neural mechanisms underlying hoverfly target detection*, and Lee presented *Edge dependence of inhibition by stationary patterns in cSIFE in the hoverfly lobula plate* at Visionarium XII, Tvärminne Zoological Station, Finland, October 2013.

A poster by Yen and **Nordström** entitled *A Novel Stationary Pattern Inhibited High-Speed Motion Sensitive Visual Neuron in the Lobula Plate* was presented at the Society for Neuroscience meeting in San Diego, December 2013.

**Nordström** gave an invited research seminar *Processing of naturalistic features in the hoverfly visual system* at the Max Planck Institute for Neurobiology, Martinsried, Germany, 2014.

**Frye** gave a plenary talk *Systems identification of visual figure detection in flies* at the Computational Neuroscience meeting (CNS): Quebec City, CN, June 2014.

Dyakova gave a poster presentation entitled *Second-order statistics of natural scenes influence object detection in hoverflies* to the Lund Vision Group, Lund University, August 2014.

**Frye** gave the Aubrey Gorbman Lecture, *Olfactory neuromodulation of motion vision behavior and circuitry in Drosophila*, Department of Biology at University of Washington, October 2014.

## 6.2 Consultative and advisory functions

Nordström acted as an academic advisor for Lee and Dyakova, and Frye for Aptekar, Kelley, and Keles, under support of the grant. Shoemaker consulted for the Frye laboratory via the Howard Hughes Medical Institute.

### 6.3 Transitions

Yu-Jen (Frank) Lee graduated from Uppsala University with a Ph.D.

Jacob Aptekar graduated from UCLA with a Ph.D., and is now a Postdoctoral Research Associate at UCLA.

Ross Kelley graduated from UCLA with a M.S., and is now a medical student at the University of Arizona.

Jessica Fox completed her postdoctoral fellowship at UCLA, and is now Assistant Professor and has started her own laboratory at Case Western Reserve University.

## 7 New Discoveries, Inventions, or Patent Disclosures

None, beyond the findings reported herein.

## 8 Honors / Awards

Jacob Aptekar: UCLA Eureka Fellowship, UCLA, 2013-2014

Nadya Zolotova: Amgen Scholar Award, 2013

Mark Frye: Plenary Speaker, International Conference on Invertebrate Vision, 2013

Mark Frye: UCLA Division of Life Science Award for Outstanding Research Publication, 2014

## References

- [1] Alger BE, Nicoll RA (1979) GABA-mediated biphasic inhibitory responses in hippocampus. *Nature* 281:315–317.
- [2] Aptekar JW, Keles MF, Mongeau J-M, Lu PM, Frye MA, Shoemaker PA (2014) Method and software for using m-sequences to characterize parallel components of higher-order visual tracking behavior in *Drosophila*. *Frontiers in Neural Circuits* 8, DOI: [10.3389/fncir.2014.00130](https://doi.org/10.3389/fncir.2014.00130).
- [3] Aptekar JW, Frye MA (2013) Higher-order figure discrimination in fly and human vision. *Current Biology* 23(16):R694-700.
- [4] Aptekar JW, Shoemaker PA, Frye MA (2012) Figure tracking by flies is supported by parallel visual streams. *Current Biology* 22:482-487.
- [5] Bahl A, Ammer G, Schilling T, Borst A (2013) Object tracking in motion-blind flies. *Nat Neurosci.* 16, 730–7388.
- [6] Bender JA, Dickinson MH (2006) Visual stimulation of saccades in magnetically tethered *Drosophila*. *J. Exp. Biol.* 209: 3170–3182.
- [7] Boeddeker N, Lindemann JP, Egelhaaf M, Zeil J (2005) Responses of blowfly motion-sensitive neurons to reconstructed optic flow along outdoor flight paths. *J Comp Physiol A* 191:1143-1155.
- [8] Borst A, Egelhaaf M (1989) Principles of visual motion detection. *Trends Neurosci* 12:297-306.
- [9] Borst A, Euler T (2011) Seeing things in motion: Models, circuits, and mechanisms. *Neuron* 71:974-994.
- [10] Borst A, Haag J, Reiff DF (2010) Fly motion vision. *Annu Rev Neurosci* 33:49-70.
- [11] Brinkworth RS, O'Carroll DC (2009) Robust models for optic flow coding in natural scenes inspired by insect biology. *PLoS Comput Biol* 5:e1000555.
- [12] Buchner E, Buchner S, Bulthoff I (1984) Deoxyglucose mapping of nervous activity induced in *Drosophila* brain by visual movement - I. Wildtype. *J. Comp. Physiol. A* 155: 471–483.

- [13] Chow DC, Theobald JC, Frye MA (2011) An olfactory circuit increases the fidelity of visual behavior. *J Neurosci* 31:15035-15047.
- [14] Chubb C, Sperling G (1988) Drift-balanced random stimuli: a general basis for studying non-Fourier motion perception. *J Opt Soc Am A* 5:1986-2007.
- [15] de Haan R, Lee Y-J, Nordström K (2013) Novel flicker-sensitive visual circuit neurons inhibited by stationary patterns. *J Neurosci* 33:8980-8989.
- [16] Duistermars BJ, Care RA, Frye MA (2012). Binocular interactions underlying the classic optomotor responses of flying flies. *Front Behav Neurosci* 6, 6.
- [17] Egelhaaf M, Hausen K, Reichardt W, Wehrhahn C (1988) Visual course control in flies relies on neuronal computation of object and background motion. *Trends Neurosci* 11:351-358.
- [18] Egelhaaf M (1985) On the neuronal basis of figure-ground discrimination by relative motion in the visual system of the fly. II. Figure-detection cells, a new class of visual interneurons. *Biol Cybern* 52:195-209.
- [19] Fischbach K-F, Dittrich P (1989) The optic lobe of *Drosophila melanogaster*. I: A. Golgi analysis of wild-type structure. *Cell Tissue Res*. 258: 441–475.
- [20] Fox JL, Aptekar JW, Zolotova NM, Shoemaker PA, Frye MA (2014) Figure-ground discrimination behavior in *Drosophila*. I. Spatial organization of wing-steering responses. *J Exp Biol* 217: 558-569.
- [21] Fox JL, Frye MA (2014) Figure-ground discrimination behavior in *Drosophila*. II. Visual influences on head movement. *J Exp Biol* 217: 570-579.
- [22] Götz KG (1968). Flight control in *Drosophila* by visual perception of motion. *Kybernetik* 4: 199–208.
- [23] Haag J, Denk W, Borst A (2004) Fly motion vision is based on Reichardt detectors regardless of the signal-to-noise ratio. *Proc. Natl. Acad. Sci. U.S.A.* 101: 16333–16338.
- [24] Hassenstein B, Reichardt W (1956) Systemtheoretische Analyse der Zeit, Reihenfolgen und Vorzeichenauswertung Bei der Bewegungserzeption des Rüsselkäfers *Chlorophanus*. *Z Naturforsch* 11: 513-524.
- [25] Hausen K (1993) The decoding of retinal image flow in insects. In: Miles FA and Wallman J (eds) *Visual Motion and its Role in the Stabilisation of Gaze*, Elsevier, London.
- [26] Heisenberg M, Wolf R (1984) *Vision in Drosophila* (Berlin: Springer-Verlag).
- [27] Jahr C, Stevens CF (1990) Voltage dependence of NMDA-activated macroscopic conductances predicted by single-channel kinetics. *Journal of Neuroscience* 10:3178–3182.
- [28] Jansonius NM, Van Hateren JH (1993) On spiking units in the 1st optic chiasm of the blowfly. III. The sustaining unit. *J Comp Physiol A* 173: 187–192.
- [29] Jansonius NM, Van Hateren JH (1991) Fast temporal adaptation of On-Off units in the 1st optic chiasm of the blowfly. *J Comp Physiol A* 168: 631–637.
- [30] Joesch M, Schnell B, Raghu SV, Reiff DF, Borst A (2010) ON and OFF pathways in *Drosophila* motion vision. *Nature* 468:300-304.
- [31] Karmeier K, van Hateren JH, Kern R, Egelhaaf M (2006) Encoding of naturalistic optic flow by a population of blowfly motion-sensitive neurons. *J Neurophysiol* 96:1602-1614.
- [32] Lee Y-J, Nordström K (2012) Higher order motion sensitivity in fly visual circuits. *Proc Natl Acad Sci USA* 109:8758-8763.
- [33] Liang P, Heitwerth J, Kern R, Kurtz R, Egelhaaf M (2012) Object representation and distance encoding in three-dimensional environments by a neural circuit in the visual system of the blowfly. *J Neurophysiol* 107: 3446-3457.
- [34] Maimon G, Straw AD, Dickinson MH (2010) Active flight increases the gain of visual motion processing in *Drosophila*. *Nat. Neurosci.* 13: 393–399.

- [35] Maimon G, Straw AD, Dickinson MH (2008) A simple vision-based algorithm for decision making in flying *Drosophila*. *Curr. Biol.* 18: 464–470.
- [36] Maisak MS, et al (2013) A directional tuning map of *Drosophila* elementary motion detectors. *Nature* 500: 212–216.
- [37] Naka KI, Rushton WAH (1966) S-potentials from luminosity units in retina of fish (*Cyprinidae*). *Journal of Physiology (London)* 185:587-599
- [38] Nordström K, Barnett PD, Moyer de Miguel IM, Brinkworth RSA, O'Carroll DC (2008) Sexual dimorphism in the hoverfly motion vision pathway. *Curr Biol* 18:661-667.
- [39] Nordström K, Barnett PD, O'Carroll DC (2006) Insect detection of small targets moving in visual clutter. *PLoS Biol* 4: 378-386
- [40] Ngo-Anh TJ, Bloodgood BL, Lin M, Sabatini BL, Maylie J, Adelman JP (2005) SK channels and NMDA receptors form a Ca<sup>2+</sup>-mediated feedback loop in dendritic spines. *Nat Neurosci* 8(5):642-649.
- [41] O'Carroll DC, Barnett PD, Nordström K (2012) Temporal and spatial adaptation of transient responses to local features. *Front Neural Circuits* 6:74.
- [42] O'Carroll DC, Barnett PD, Nordström K (2011) Local and global responses of insect motion detectors to the spatial structure of natural scenes. *J Vis* 11: 20.
- [43] Osorio D (1991) Mechanisms of early visual processing in the medulla of the locust optic lobe: How self-inhibition, spatial-pooling, and signal rectification contribute to the properties of transient cells. *Vis Neurosci* 7:345-355.
- [44] Otsuna H, Ito K (2006) Systematic analysis of the visual projection neurons of *Drosophila melanogaster*. I. Lobula-specific pathways,” *J. Comp. Neurol.* 497:928–958.
- [45] Quenzer T, Zanker JM (1991) Visual detection of paradoxical motion in flies. *J Comp Physiol A* 169:331-340.
- [46] Reichardt W, Poggio T (1979) Figure-ground discrimination by relative movement in the visual-system of the fly. Part I: Experimental results. *Biol Cybern* 35:81-100.
- [47] Sanders H, Berends M, Major G, Goldman MS, Lisman JE (2013) NMDA and GABAB (KIR) conductances: the “perfect couple” for bistability. *Journal of Neuroscience* 33:424–4299.
- [48] Schilstra C, van Hateren JH (1998). Stabilizing gaze in flying blowflies. *Nature* 395, 654.
- [49] Shoemaker PA (2011) Neural bistability and amplification mediated by NMDA receptors: analysis of stationary equations. *Neurocomputing* 74:3058–3071.
- [50] Single S, Borst A (1998) Dendritic integration and its role in computing image velocity. *Science* 281: 1848–1850.
- [51] Strausfeld NJ, Sinakevitch I, Okamura J-Y (2007) Organization of local interneurons in optic glomeruli of the dipterous visual system and comparisons with the antennal lobes.,” *Dev. Neurobiol* 67:1267–1288.
- [52] Strausfeld NJ, Okamura J-Y (2007) Visual system of calliphorid flies: organization of optic glomeruli and their lobula complex efferents. *J. Comp. Neurol.* 500:166–188.
- [53] Strausfeld NJ, Douglass JK, Campbell H, Higgins C (2006) Parallel processing in the optic lobes of flies and the occurrence of motion computing circuits., in *Invertebrate Vision*, 2006, pp. 349–398.
- [54] Takemura S-Y, et al. (2013) A visual motion detection circuit suggested by *Drosophila* connectomics. *Nature* 500.7461: 175-181.
- [55] Theobald JC, Shoemaker PA, Ringach DL, Frye MA (2010) Theta motion processing in fruit flies. *Frontiers in Behavioral Neuroscience*, DOI: [10.3389/fnbeh.2010.00035](https://doi.org/10.3389/fnbeh.2010.00035).
- [56] Theobald JC, Ringach DL, Frye MA (2010) Dynamics of optomotor responses in *Drosophila* to perturbations in optic flow. *J Exp Biol* 213, 1366-1375.



- [57] Theobald JC, Duistermars BJ, Ringach DL, and Frye MA (2008). Flies see second-order motion. *Current Biology* 18, R464-465.
- [58] van Breugel F, Dickinson MH (2012) The visual control of landing and obstacle avoidance in the fruit fly *Drosophila melanogaster*. *J. Exp. Biol.* 215: 1783–1798.
- [59] Wiederman SD, Shoemaker PA, O’Carroll DC (2013) Correlation between OFF and ON channels underlies dark target selectivity in an insect visual system. *Journal of Neuroscience* 33, pp 13225-13232.
- [60] Wiederman SD, Shoemaker PA, O’Carroll DC (2008) A model for the detection of moving targets in visual clutter inspired by insect physiology. *PLoS ONE*, Vol. 3(7): e2784. DOI: [10.1371/journal.pone.0002784](https://doi.org/10.1371/journal.pone.0002784)
- [61] Zanker JM (1994) Modelling human motion perception. II. Beyond Fourier motion stimuli. *Naturwissenschaften* 81:200-209.
- [62] Zanker JM (1993) Theta motion: a paradoxical stimulus to explore higher order motion extraction. *Vision Res* 33:553-569.